



# Optimizing Interface Conductivity in Electronics



The latest eBook from  
**Advanced Optical Metrology.**  
Download for free.

Surface roughness is a key parameter for judging the performance of a given material's surface quality for its electronic application. A powerful tool to measure surface roughness is 3D laser scanning confocal microscopy (LSM), which will allow you to assess roughness and compare production and finishing methods, and improve these methods based on mathematical models.

Focus on creating high-conductivity electronic devices with minimal power loss using laser scanning microscopy is an effective tool to discern a variety of roughness parameters.

**EVIDENT**  
**OLYMPUS**

**WILEY**

# A Metal–Organic Framework Incorporating Eight Different Size Rare-Earth Metal Elements: Toward Multifunctionality *À La Carte*

Zhen Li, Xiao-Bao Li, Mark E. Light, Anna E. Carrillo, Ana Arauzo, Manuel Valvidares, Claudio Roscini, Francesc Teixidor, Clara Viñas, Felipe Gándara, Elena Bartolomé,\* and José Giner Planas\*


Multi-metallic multivariate (MTV) rare earth (RE) metal–organic frameworks (MOFs) are of interest for the development of multifunctional materials, however examples with more than three RE cations are rare and obstructed by compositional segregation during synthesis. Herein, this work demonstrates the synthesis of a multi-metallic MTV RE MOF incorporating two, four, six, or eight different RE ions with different sizes and in nearly equimolar amounts and no compositional segregation. The MOFs are formed by a combination of RE cations (La, Ce, Eu, Gd, Tb, Dy, Y, and Yb) and a 1,7-di(4-carboxyphenyl)-1,7-dicarba-closo-dodecaborane (*mCB-L*) linker. The steric bulkiness and acidity of *mCB-L* is crucial for the incorporation of different size RE ions into the MOF structure. Demonstration of the incorporation of all RE cations is performed via compositional and structural characterization. The more complex MTV MOF, including all eight RE ions (*mCB-8RE*), are also characterized using optical, thermal, and magnetic techniques. Element-selective X-ray absorption spectroscopy and X-ray Magnetic Circular Dichroism measurements allow us to characterize spectroscopically each of the eight RE ions and determine their magnetic moments. This work paves the way for the investigation of MTV MOFs with the possibility to combine RE ions *à la carte* for diverse applications.

## 1. Introduction

Across various domains, the presence of materials incorporating multiple metal elements is essential. This is because the integration of different metal cations often leads to the emergence of novel or improved properties that cannot be achieved by employing a single metal alone. In the field of alloys, the advent of a new alloy design concept based on multi-components (5 or more transition metals)<sup>[1,2]</sup> has opened a flurry of research interest from all over the world.<sup>[3,4]</sup> None of these research would have been possible without the ability to synthesize “compositionally complex materials” in the first place. In this sense, the addressable combination of multiple metal elements remains a major synthetic challenge in the field of metal-organic frameworks.<sup>[5–7]</sup> MOFs are a type of materials constructed through the combination of organic linkers and metal ions into periodic, extended structures. In the particular case of

Z. Li, X.-B. Li, A. E. Carrillo, F. Teixidor, C. Viñas, J. G. Planas  
Inorganic Materials and Catalysis Laboratory (LMI)  
Institut de Ciència de Materials de Barcelona (ICMAB-CSIC)  
Campus UAB, Bellaterra 08193, Spain  
E-mail: jginerplanas@icmab.es

Z. Li  
Shandong Provincial Key Laboratory of Monocrystalline Silicon Semiconductor Materials and Technology  
College of Chemistry and Chemical Engineering  
Dezhou University  
Dezhou 253023, China

 The ORCID identification number(s) for the author(s) of this article can be found under <https://doi.org/10.1002/adfm.202307369>

© 2023 The Authors. Advanced Functional Materials published by Wiley-VCH GmbH. This is an open access article under the terms of the Creative Commons Attribution License, which permits use, distribution and reproduction in any medium, provided the original work is properly cited.

DOI: 10.1002/adfm.202307369

M. E. Light  
Department of Chemistry  
University of Southampton  
Highfield, Southampton SO17 1BJ, UK

A. Arauzo  
Instituto de Nanociencia y Materiales de Aragón (INMA)  
Departamento de Física de la Materia Condensada  
CSIC-Universidad de Zaragoza  
Zaragoza 50009, Spain

M. Valvidares  
ALBA Synchrotron Light Source  
Cerdanyola del Vallès  
Barcelona 08290, Spain

C. Roscini  
Catalan Institute of Nanoscience and Nanotechnology (ICN2)  
CSIC  
and Barcelona Institute of Science and Technology (BIST)  
Bellaterra, Barcelona 08193, Spain



multi-metal multivariate (MTV) MOFs, different metal elements occupy topologically equivalent positions in the secondary building units (SBUs), without altering the network connectivity as compared to that of their single-metal counterparts.<sup>[5,8–10]</sup> All these materials manifest an increased complexity, which can provide a new generation of materials with diverse properties. Thus, the combination of different metal cations in MOF structures introduces “heterogeneity within order,”<sup>[11,12]</sup> as the spatial arrangement of metal atoms might vary within an ordered and symmetric backbone (Sequencing in **Figure 1**). Such MTV MOF materials show photo-<sup>[13]</sup> electro-<sup>[14,15]</sup> catalytic<sup>[16,17]</sup> or luminescence properties<sup>[18,19]</sup> and are emerging as supercapacitor candidates<sup>[20,21]</sup> among other applications.<sup>[22]</sup> However, the greater the number of elements to be combined, the more challenging and difficult is their judicious incorporation and characterization of the MOF structure.<sup>[5]</sup> Nevertheless, such complexity has been achieved in the case of transition metals, and multi-metal MTV MOFs, where structures incorporating up to ten different transition metals elements have been synthesized.<sup>[6,9,14,15,23–28]</sup> Interestingly, for the case of the 10 metal MOF-74 it was already recognized that the preferential incorporation of some elements over others leads to an inhomogeneous metal distribution and prevents precise control of the metal ratios. More recently, Yaghi and coworkers have reported the precise sequence of two metals within the MOF-74 structure by atom probe tomography,<sup>[29]</sup> finding different types of metal sequencing depending on the reaction temperature, and demonstrating that the spatial distribution of the different metal elements is governed by the different sets of synthetic conditions. Moreover, their ratio cannot be precisely controlled due to the more restricted coordination environment of these d-metals.<sup>[5,30]</sup> These results emphasize the lack of uniformity in the distribution of metals within transition metals MTV MOFs, highlighting the inhomogeneity of metal mixing.

In the case of rare-earth (RE) MOFs, high homogeneity can be found in the corresponding MTV MOFs when mixing two metal cations of similar size. The quite similar coordination numbers of RE ions has facilitated the incorporation at various ratios (e.g., 1% increments) of two or three RE metals of close sizes.<sup>[30,31]</sup> However, at present there are no existing MTV MOFs with a high number of RE metals.<sup>[32]</sup> RE elements refer to the 15 lanthanide elements, scandium and yttrium. Due to their particular electron configuration (gradual filling of their 4f orbitals from La<sup>3+</sup> to Lu<sup>3+</sup>), RE element-based materials display unique properties with interest in diverse fields such as energy conversion,<sup>[33–35]</sup> catalysis,<sup>[34,36]</sup> luminescence,<sup>[37,38]</sup> or magnetism.<sup>[39]</sup> In particular, the electronic properties of trivalent Ln(III) lanthanides make them ideal for the design of both luminescent materials<sup>[40–43]</sup> and

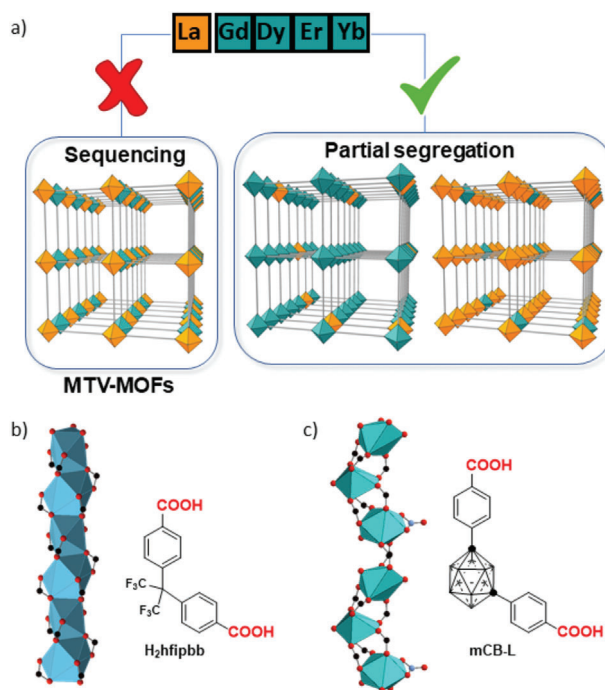


**Figure 1.** Outcomes in the competitive formation of crystals with various bimetallic combinations and rod-shape SBU examples. a) Combination of different size rare earth metal cations in rod-shaped SBUs constructed from dicarboxylated linkers results in preferential partial segregation. b) One rod SBU of RPF-4 composed of mono-metallic LnO<sub>9</sub> polyhedra sharing faces (Ln = Yb or La) by H<sub>2</sub>hfpdd linker. c) one rod SBU of mCB-L composed of LnO<sub>x</sub> (x = 8–9) polyhedra sharing vertices by mCB-L linker.

single-molecule magnets (SMMs).<sup>[44–46]</sup> At present, great efforts are being made to develop molecular systems coordinating different RE ions, as their combination can be used in many applications, for example, for anticounterfeiting,<sup>[47]</sup> as thermometric probes,<sup>[48,49]</sup> to improve up-conversion efficiency,<sup>[50]</sup> to modify the color or brightness of emission in luminescent systems,<sup>[51,52]</sup> to produce contrast agents,<sup>[53]</sup> or in the field of quantum computing, for the realization of qubits and qugates,<sup>[54–56]</sup> spin valves,<sup>[57]</sup> or to perform quantum error correction protocols.<sup>[58,59]</sup> In some of the above applications, the coexistence of RE cations of significantly varying sizes is of utmost importance. This achievement remains elusive for MOFs, and has so far been limited to discrete complexes, wherein linkers with distinct coordination pockets—a smaller one and a larger one—are employed.<sup>[55,56]</sup>

Although RE MOFs are in principle particularly favorable for the preparation of MTV MOFs due to their similar reactivity and coordination environments,<sup>[10]</sup> the majority of the reported materials comprise only two metals (e.g., Eu<sup>3+</sup> and Tb<sup>3+</sup>),<sup>[21]</sup> with a few exceptions having three.<sup>[10,18,19,60,61]</sup> In general, cations of similar size can replace one another in inorganic materials and therefore can be incorporated simultaneously within the crystal.<sup>[31]</sup> However, incorporation of different size RE cations is more challenging. In this regard, research results, including our own, have revealed that despite their similar coordination chemistry behavior, when it comes to MOF synthesis, reactions with different lanthanide elements might lead to different crystallization pathways even to produce the same structure type known for

F. Gándara  
Fronteras en Química de Materiales  
Materials Science Institute of Madrid-Spanish National Research Council (ICMM-CSIC)  
Madrid 28049, Spain  
E. Bartolomé  
EUSS Research Group  
Escola Universitària Salesiana de Sarrià (EUSS)  
Passeig Sant Joan Bosco, 74, Barcelona 08017, Spain  
E-mail: ebartolome@euss.es

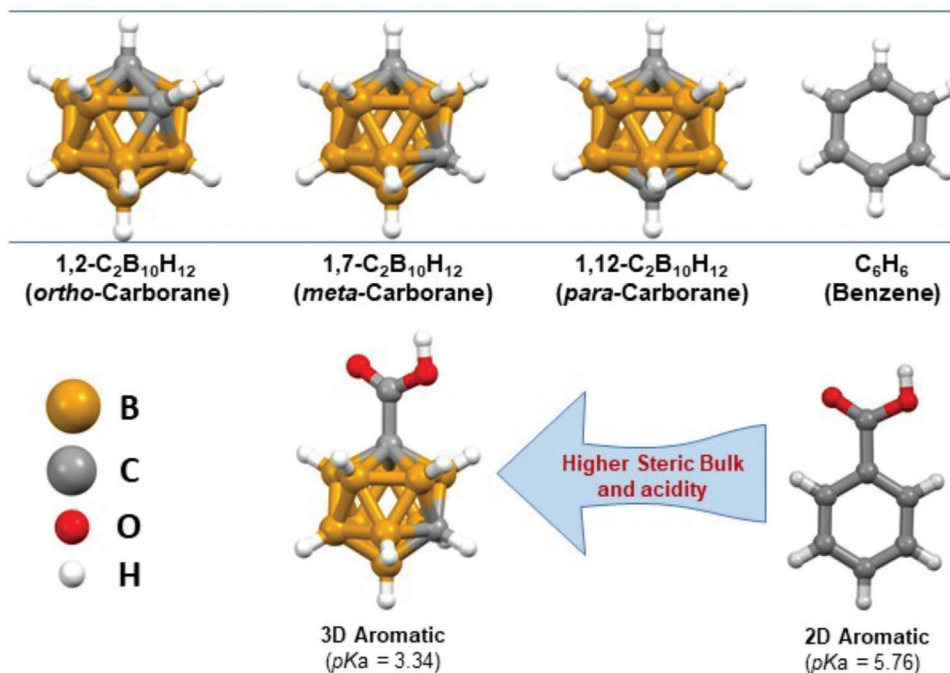


**Figure 2.** Comparison of molecular structures of icosahedral dicarba-*closo*-dodecaboranes (carboranes) with benzene and acidities of carboxylic derivatives.

the individual, single-metal RE-MOFs (Figure 1a).<sup>[62]</sup> Thus, the synthetic and crystallization study carried out with the rare-earth polymeric framework (RPF-4) family, which consists of a rod SBU and a V-shaped fluorinated organic linker, demonstrated that some binary RE combinations result in compositional segregation of crystals, while others allow the formation of RE MTV MOFs with controllable metal arrangements. Particularly, the inorganic SBU in the RPF-4 family comprises REO<sub>9</sub> polyhedra that share faces via three  $\mu$ -O atoms, resulting in short distances between RE elements, ranging from 3.6 to 3.9 Å (Figure 1b).

While rod-shaped SBUs are commonly encountered in MOFs,<sup>[63]</sup> the distance between metal elements in the rods depends on the different coordination modes of the carboxylate groups, which in turn is imposed by the employed organic linker. In this sense, we have recently reported a RE-MOF family with the carborane-based linker 1,7-di(4-carboxyphenyl)-1,7-dicarba-*closo*-dodecaborane (*mCB-L*).<sup>[64]</sup> Icosahedral carboranes 1,*n*-C<sub>2</sub>B<sub>10</sub>H<sub>12</sub> (*n* = 2, 7 or 12; **Figure 2**), are a class of commercially available and exceptionally stable 3D-aromatic boron-rich clusters<sup>[65–67]</sup> that possess material-favorable properties such as thermal/chemical stability and high hydrophobicity.<sup>[68–74]</sup> The spherical nature of the *closo*-carboranes, with slightly polarized hydrogen atoms and the presence of the hydride-like hydrogens at the B-H vertexes, make the carboranes very hydrophobic. Carborane-based MOFs are known<sup>[75–82]</sup> and research, including our own work, has shown that the incorporation of hydrophobic carborane linkers into the MOF frameworks increases their hydrolytic stabilities.<sup>[64,83–88]</sup> Beyond stability, the delocalized electron density is not uniform through the *icosahedral closo*-carborane cages, giving rise to extraordinary differences in the electronic effects of the cluster.<sup>[89]</sup> This unusual electronic structure is often highlighted by considering carboranes as inorganic

3D “aromatic” analogs of arenes.<sup>[65–67]</sup> It is therefore common to compare carboranes with benzene.<sup>[90,91]</sup> The former are significantly larger ( $\approx 40\%$ ) than the benzene ring rotation envelop.<sup>[69]</sup> Carboranes behave as strong electron-withdrawing groups (similar to a fluorinated aryl) on a substituent at one of the cluster carbons.<sup>[69,92–94]</sup> Thus, the carboxylic derivatives of carboranes (Figure 2; *pKa* values *o*-carborane, 2.64; *m*-carborane 3.34, *p*-carborane 3.64) are more acidic than the corresponding benzoic acid (*pKa* 5.76).<sup>[95]</sup> Our *mCB-Ln* MOF family was originally reported with the use of Eu and Tb, and also with their multi-metal Eu/Tb combination.<sup>[64]</sup> In all cases, single-crystal X-ray diffraction (SCXRD) showed a structure formed by rod-shaped SBUs, which are formed by vertex-sharing REO<sub>*x*</sub> (*x* = 8–9) polyhedra. When compared to the RPF-4 series (Figure 1b,c),<sup>[96]</sup> a close inspection to the SBUs shows a considerably larger metal – metal distance along the rod SBU in the *mCB-Tb* MOF (Tb–Tb: 4.640, 4.583, and 5.255 Å) than in RPF-4 family (La–La: 3.896 Å; Yb–Yb: 3.661 Å). We reasoned that this much larger RE–RE distance in our carborane MOF could provide a more favorable scenario to accommodate a number of different RE cations with dissimilar radii, and therefore facilitate the preparation of a MTV MOFs with a large number of different metal elements.

Thus, in the present work, we report a linker-directed synthesis approach that enables the direct integration of two to eight rare-earth metal elements into a single structure. This method enables control over the number and size of metal cations (La<sup>3+</sup>, 1.250 Å; Ce<sup>3+</sup>, 1.220 Å; Eu<sup>3+</sup>, 1.120 Å; Gd<sup>3+</sup>, 1.105 Å; Tb<sup>3+</sup>, 1.090 Å; Dy<sup>3+</sup>, 1.075 Å; Y<sup>3+</sup>, 1.011 Å and Yb<sup>3+</sup>, 1.010 Å),<sup>[97,98]</sup> and in a nearly equimolar ratio within the resulting material. The choice of linker and initial molar ratio of the metal elements employed governs the incorporation of the metal components within the MOF structure. The synthesis, structural, optical, magnetic and



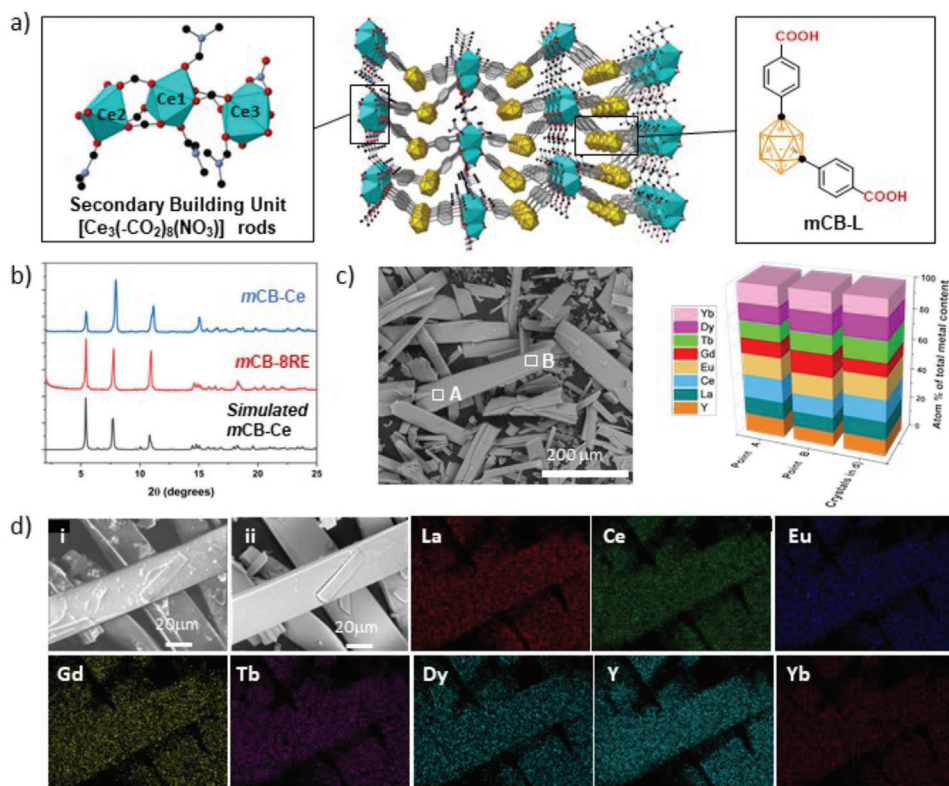


**Figure 3.** Crystal structures of *mCB-Ce*, *mCB-8RE* (La, Ce, Eu, Gd, Tb, Dy, Y, and Yb) and illustration of homogeneous metal mixing in *mCB-8RE*. a–d) Crystal structure of single-metal *mCB-Ce*, showing the construction of the 3D structure from the rod-shaped SBUs and the carborane linker *mCB-L* (a). Blue and yellow polyhedra represents the Ce coordination spheres and icosahedral *closo*-carboranes, respectively. H atoms are omitted for clarity. Color code: B, orange; C, gray; O, red; N, dark blue; Ce, blue. Three independent metal atoms (SBU) are repeated along the structure to provide 1D inorganic rod-shaped chains that are bridged by the carborane linker to form the observed 3D structures. b) PXRD patterns of experimental *mCB-Ce* (blue) and *mCB-8RE* (red) and simulated *mCB-Ce* (black), demonstrating phase purity and isostructurality. c) SEM image of *mCB-8RE* and EDX analysis of point scans of the RE metals on the indicated positions (A and B) in one crystal and on multiple crystals shown in (d). SEM images (secondary (i) and backscattered (ii) electrons) and EDX mapping of the same sample area, demonstrating the presence of each of the 8 RE metals in *mCB-8RE*.

thermal characterization of the more complex multivariate MOF containing eight different rare earths is presented. We discuss the possible reasons for the formation and stability of this MTV MOF and how we could modulate the intermetallic distances by choosing the appropriate ligand steric bulkiness. The possibility of introducing multiple numbers of different RE<sup>3+</sup> cations, each having distinct luminescence or magnetic properties, and with different sizes, paves the way for the investigation of the fundamental properties of multi-metallic MOFs and the preparation of multifunctional MOFs with customized properties.

## 2. Results and Discussion

### 2.1. Synthesis and structural characterization

We first synthesized and characterized the single-metal *mCB-RE* samples for a wide variety of ionic radii RE elements (RE = La, Ce, Gd, Dy, Y, or Yb), that together with the previously reported Eu and Tb MOFs (*mCB-Eu* and *-Tb*),<sup>[64]</sup> covers most possible ionic radii sizes in the RE series. The solid-state structure for single-metal *mCB-Tb*<sup>[64]</sup> and *mCB-Ce* (Table S1 and Figure S1, Supporting Information) have been determined by SCXRD. Figure 3 shows a representation of the solid-state structure for

*mCB-Ce* which, as expected, is isostructural with that of *mCB-Tb* (Figure S2, Supporting Information). These two MOFs crystallize in the monoclinic *Pn* space group and analysis of the structure revealed the formation of a 3D framework based on a [(RE)<sub>3</sub>(-COO)<sub>8</sub>(NO<sub>3</sub>)(O<sub>DMF</sub>)<sub>x</sub>] (*x* = 4 (Tb), 5 (Ce); DMF = N,N-Dimethylformamide) SBU (Figures 1, 3 and Figure S2, Supporting Information). As in the Tb structure, the SBU of *mCB-Ce* is composed of 3 non-equivalent crystallographic metal atoms, which are linearly arranged and capped by bridging or chelate-bridging *mCB-L*, chelate NO<sub>3</sub><sup>-</sup> and DMF molecules. Whereas one of the Ce atoms in the SBU is in a CeO<sub>9</sub> coordination environment, the other two are in a CeO<sub>8</sub> environment (Figure 3a and Figure S1, Supporting Information). Similarly, as observed in the Tb structure, the Ce–Ce distances in *mCB-Ce* (4.63–5.25 Å) are considerably larger than those in other rod-shaped Ce structures described in the literature.<sup>[99,100]</sup> A decrease of the cell parameters from the *mCB-Ce* (Table S1, Supporting Information) to the *mCB-Tb*<sup>[64]</sup> structures is observed, being consistent with the corresponding decrease in ionic radii.<sup>[101]</sup> Powder X-ray diffraction (PXRD) (Figure S3, Supporting Information) and Fourier Transform Infrared (FT-IR) spectroscopy (Figure S4, Supporting Information) confirmed that all eight single-metal *mCB-RE* compounds (RE = La, Ce, Eu, Gd, Tb, Dy, Y, or Yb) are structurally

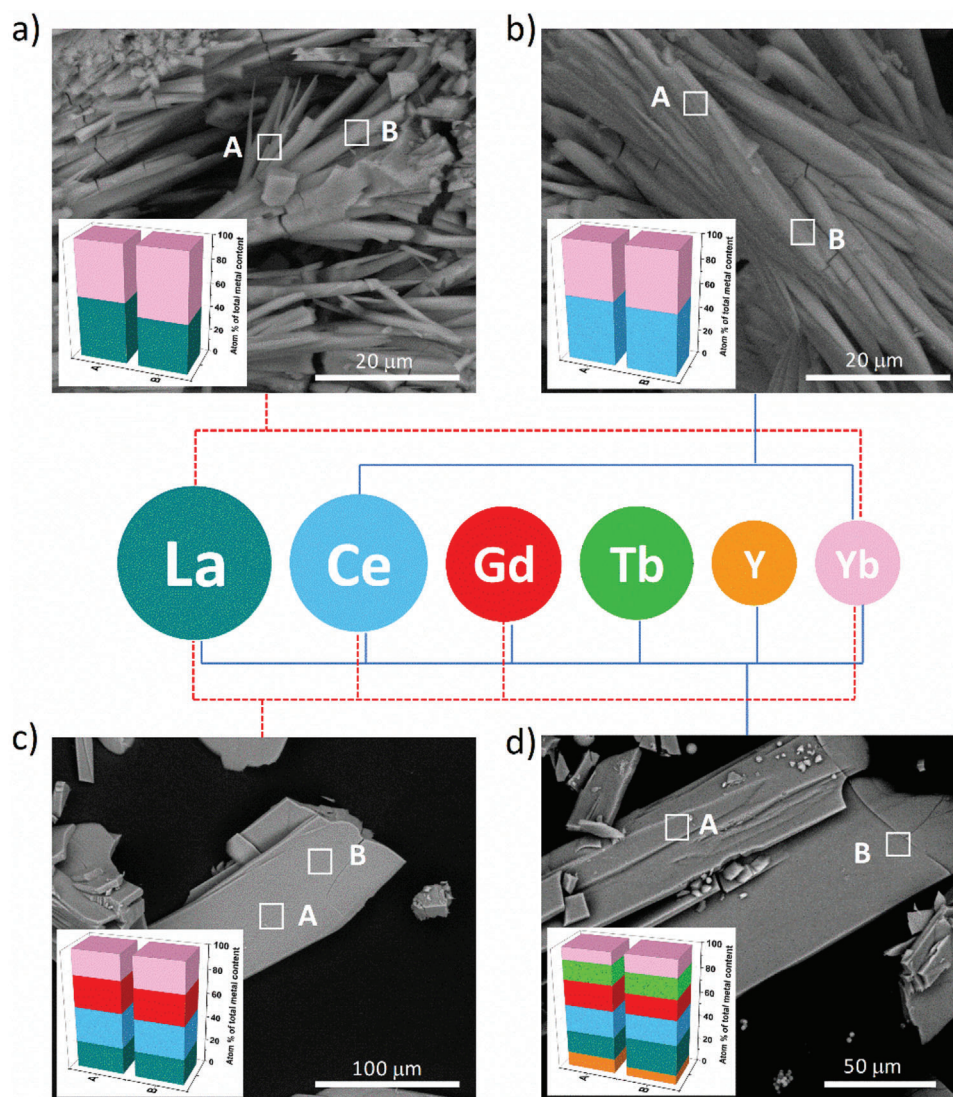


**Figure 4.** SEM images of *mCB-nRE-MOF* ( $n = 2$  (La and Yb),  $2'$  (Ce and Yb),  $4$  (La, Ce, Gd and Yb), and  $6$  (La, Ce, Gd, Tb, Y, and Yb) and illustration of their homogeneous metal mixing and cations relative sizes. a–d) SEM images of crystal samples for *mCB-2RE-MOF* (a), *mCB-2'RE-MOF* (b), *mCB-4RE-MOF* (c), and *mCB-6RE-MOF* (d), showing the regions on which EDX analyses were taken (A and B) and the plot of ratio of metals (%; insets), found in each region, demonstrating the presence of each metal in nearly equimolar ratio.

identical. The coincidence between their experimental PXRD pattern (Figure S3, Supporting Information) and the one calculated for the single-crystal structure of *mCB-Tb*<sup>[64]</sup> and *mCB-Ce* (Figure 3b) proves that they present the same crystal structure.

Once confirmed that all single-metal *mCB-RE* materials display the same crystal structure consisting of rod-shaped  $\text{REO}_n$  ( $n = 8-9$ ) polyhedra sharing vertexes, with significantly larger RE-RE distances than those of the related RPF-4 materials (Figure 1b),<sup>[96]</sup> we continued our study into the possibility of preparing a multi-metal RE MTV MOFs. Solvothermal synthesis of *mCB-L* linker with a mixture of eight rare earth metal salts ( $\text{RE}(\text{NO}_3)_3 \cdot x\text{H}_2\text{O}$ ,  $\text{RE} = \text{La, Ce, Eu, Gd, Tb, Dy, Y, Yb}$ ; Methods and Supporting Information) provided colorless crystals of  $\{[(\text{La}_{0.07}\text{Ce}_{0.11}\text{Eu}_{0.13}\text{Gd}_{0.11}\text{Tb}_{0.11}\text{Dy}_{0.13}\text{Y}_{0.20}\text{Yb}_{0.14})_3(\text{mCB-L})_4(\text{NO}_3)(\text{DMF})_x]_n \cdot \text{Solv}\}$  (*mCB-8RE*). This RE MTV MOF shows a crystal habit similar to that of the individual and bimetal

counterparts  $\{[(\text{RE})_3(\text{mCB-L})_4(\text{NO}_3)(\text{DMF})_x]_n \cdot \text{Solv}\}$  (*mCB-RE*, where  $\text{RE} = \text{Eu, Tb, or Eu}_x\text{Tb}_{1-x}$ ) (Figure S5, Supporting Information).<sup>[64]</sup> Powder X-ray diffraction data for *mCB-8RE* crystals (Figure 3b and Figure S3, Supporting Information) revealed that the material is also isostructural with all above *mCB-RE* MOF materials. The chemical composition of the *mCB-8RE* bulk sample was determined by means of inductively coupled plasma (ICP) measurements and elemental analysis. The ICP results reveal a nearly equimolar ratio of Ce, Eu, Gd, Tb, Dy, and Yb, whereas that for the largest metal La is slightly smaller and that for Y is slightly larger. These data confirm that all eight RE metals are effectively incorporated into the MOF structure by one-pot solvothermal synthesis. Element selective X-ray absorption spectroscopy (XAS) also confirmed the presence of all metals in the crystals (vide infra). Scanning electron microscopy (SEM)/Energy dispersive X-ray (EDX) spectroscopy



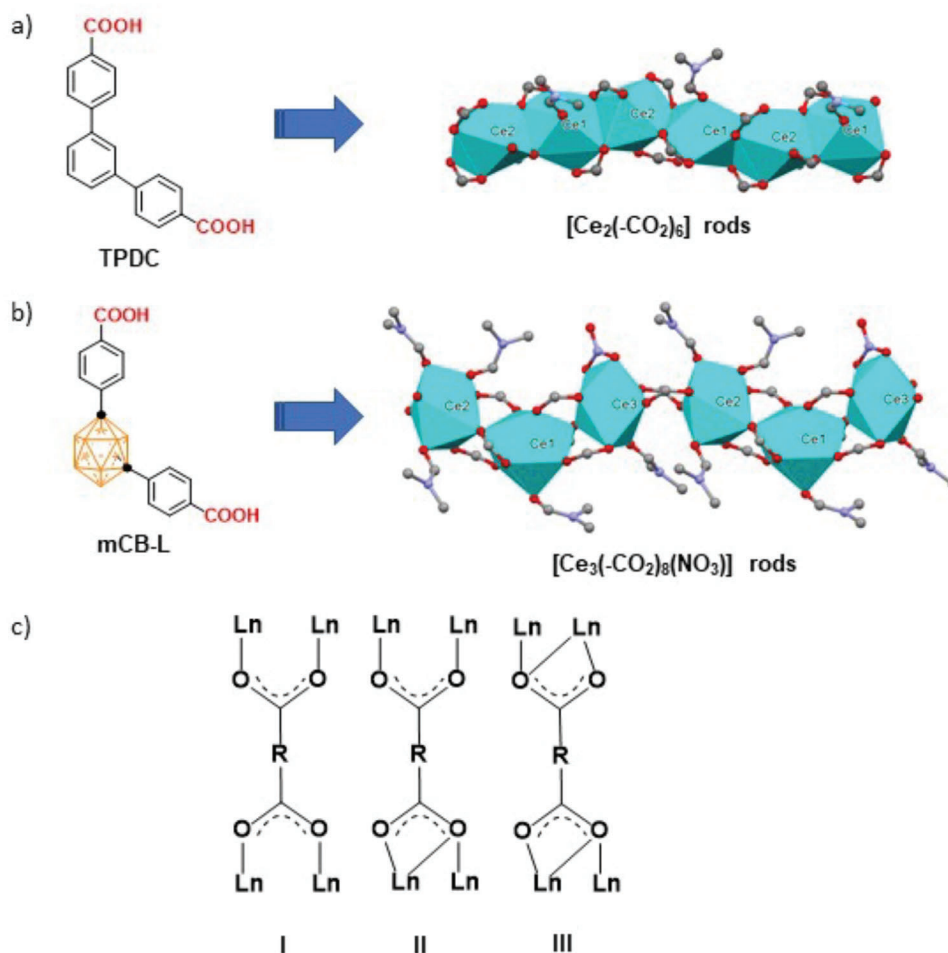


**Figure 5.** Comparison of rod-shaped SBUs for TPDC-Ce, mCB-Ce and illustration of carboxylates binding. a) TPDC linker and the 1D inorganic rod-shaped chains that are bridged by the linker in the SCXRD for **TPDC-Ce**. b) 1D inorganic rod-shaped chains that are bridged by the **mCB-L** linker in the SCXRD for **mCB-Ce**. Blue polyhedra represents the Ce coordination spheres. Color code: C, gray; O, red; N, dark blue; Ce, blue. c) Dicarboxylates bringing modes found in **TPDC-Ce** and **mCB-Ce**.

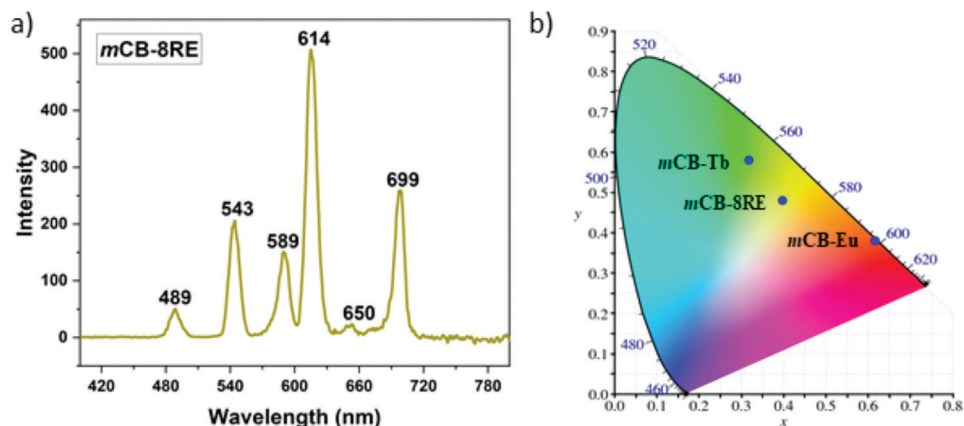


**Figure 6.** Optical and photophysical properties for **mCB-8RE** (La, Ce, Eu, Gd, Tb, Dy, Y, Yb). a) Emission spectrum of **mCB-8RE** ( $\lambda_{ex} = 280$  nm); b) Color coordinates drawn onto the 1931 CIE chromaticity diagram for **mCB-Tb**, **mCB-Eu**, and **mCB-8RE**.

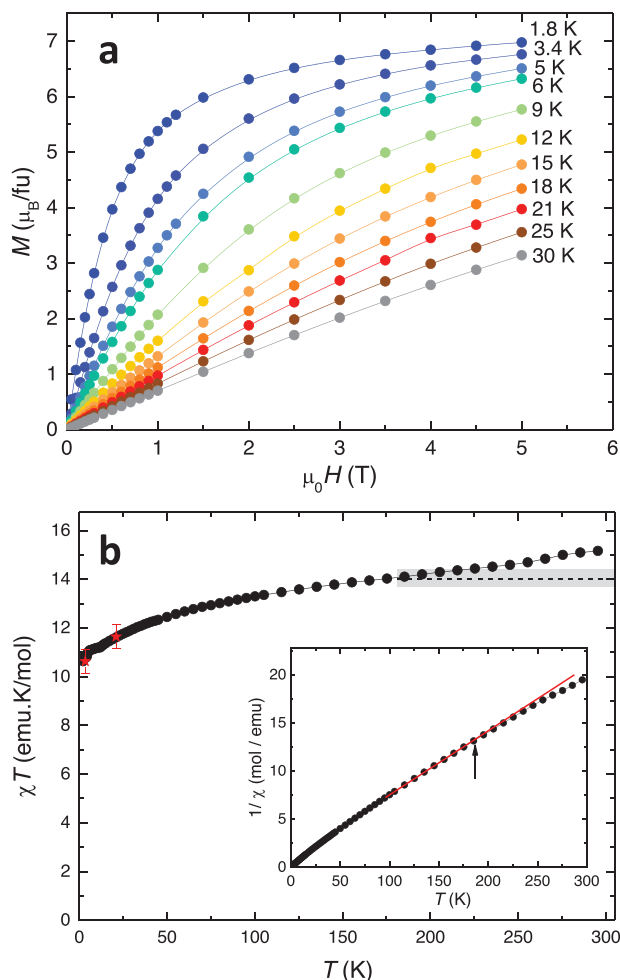


**Figure 7.** Dc magnetometry of *mCB-8RE*. a) Field-dependence of the magnetization,  $M(H)$ , at different temperatures between  $T = 1.8$ – $30$  K ( $M_w = 2297.43$  g mol $^{-1}$ ); b) temperature dependence of the susceptibility-temperature,  $\chi T(T)$ , at  $\mu_0 H = 1$  T. The dashed line signals the high- $T$  constant saturation value expected for the combination of Tb $^{3+}$ , Dy $^{3+}$ , Gd $^{3+}$ , Yb $^{3+}$ , Ce $^{3+}$ , and Eu $^{2+}$  ions, in the proportions found from ICP and XAS; the increasing  $\chi T$  above  $\approx 190$  K is owed to the non-linear Eu $^{3+}$  contribution (the grey shaded region is the error bar). The star symbols represent the  $\chi T$  values obtained at 3.4 and 21 K from XMCD/ $H$  data. Inset, right: inverse of the susceptibility,  $1/\chi$ .

was used to further investigate the distribution of the different metals in the material. Figure 3c,d shows the SEM/EDX mapping of crystals of the as-synthesized *mCB-8RE*, showing that the different RE metals are uniformly distributed within the area of the crystals and are not a physical mixture of different metal compounds. Moreover, all analyzed crystals displayed similar metal ratios, demonstrating that the sample has a homogeneously distributed composition, ruling out the compositional segregation scenario (Figure 1a). A similar brightness in the EDX mapping for all metals suggests their nearly equal contents in the MOF, being consistent with the ICP results. The overall data confirms that the eight RE metals are dispersed in the MOF lattice.

The thermal decomposition processes of the single-metal *mCB-RE* and the multi-metallic *mCB-8RE* were comparatively

investigated via thermogravimetric analysis (TGA) in the wide temperature range from 25 to 800 °C (Figure S6, Supporting Information). The TGA analysis indicates that all materials undergo two processes during the heating: loss of the solvent (coordinated to metal sites and/or distributed in the pores) in the range 200–350 °C and decomposition of the framework above 500 °C. Decomposition temperatures for all single-metal materials (525–538 °C) and multi-metal material (532 °C) are rather uniform, showing a quite similar thermodynamic stability. All the above data confirmed the chemical composition of the single-metal, *mCB-RE*, and the multi-metal RE MTV MOF, *mCB-8RE*. The amount of both coordinated and uncoordinated DMF and H $_2$ O vary in the family of compounds. The high variability in the solvation is consistent with a dynamic solvation structure of lanthanides<sup>[102]</sup> that is further complicated with the inclusion of solvent in the framework voids. Sorption measurements after thermal activation (removal of solvent in the voids by thermal treatment under high vacuum) revealed that all compounds are non-porous to N $_2$  but porous to CO $_2$  with Dubini–Radushkevich surface areas ranging from 147 to 331 m $^2$  g $^{-1}$  (Figure S7, Supporting Information).

As mentioned above, Gándara and coworkers found that for certain binary combinations of RE metals, particularly those involving the combination of lanthanum with elements other than cerium, compositional segregation was observed (Figure 1a), while for other cases the binary RE MTV systems were successfully obtained. Differences in the crystallization mechanism, as well as thermodynamic effects were proposed to be responsible for the differently observed behavior.<sup>[62]</sup> So the question arises as to how is it possible that we could now incorporate eight different RE metals with nearly equimolar concentration and covering all possible ionic radii sizes? A systematic crystallization study is discarded in the present case considering the large, unmanageable amount of experimental data required for all possible metal combinations involving eight different metal elements. However, we have selected a few cation combinations, keeping the largest and smallest size cations in each combination, in order to confirm the generality of the proposed synthetic strategy. Consequently, we have prepared the following series of RE MTV MOFs, *mCB-nRe-MOF* ( $n = 2$  (La and Yb), 2' (Ce and Yb), 4 (La, Ce, Gd, and Yb), and 6 (La, Ce, Gd, Tb, Y, and Yb), with all cations in equimolar ratio. We have structurally characterized all new compounds by PXRD and the crystals analyzed by SEM-EDX (Experimental, Figure 4, Figures S8 and S9, Supporting Information). The results confirmed the isostructurality of all compounds and proved that all metals in each material are introduced in a nearly equimolar ratio, even for the binary La-Yb and Ce-Yb combination (Figure 4a,b and Figure S9, Supporting Information). The observation of the same crystal habit for all single-metal and multi-metal materials suggests that a similar crystallization mechanism is followed for all elements, and therefore it does not play a crucial role in this case.

It is important to remark that the coordination chemistry of RE-metals is very diverse, with only small energetic differences between different coordination numbers and geometries, and where coordination geometry is dictated primarily by ligand and steric effects, as interactions are electrostatic in nature.<sup>[101,103]</sup> This is a consequence of the shielding of the 4f electrons by the 5s<sup>[2]</sup> and 5p<sup>[6]</sup> orbitals, which makes the electrons poorly



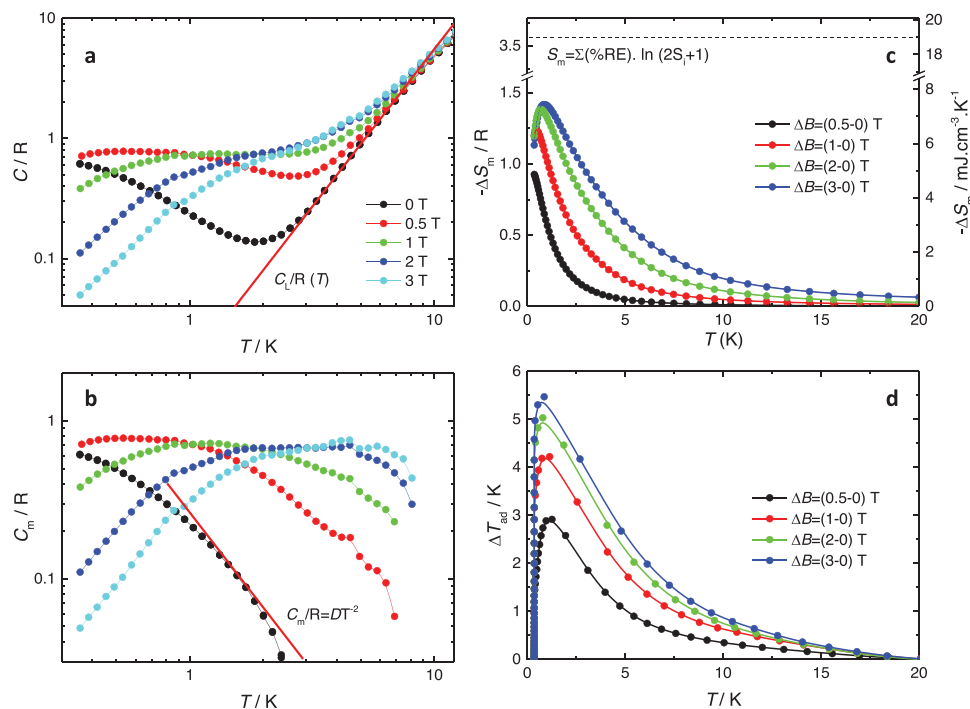


**Figure 8.** Heat capacity and magnetocaloric effect of **mCB-8RE**. a) Temperature dependence of the heat capacity at different applied magnetic fields,  $C(T, H)$ , normalized to the ideal gas constant  $R = 8.314 \text{ J mol}^{-1} \text{ K}^{-1}$ . The line corresponds to the lattice contribution,  $C_L/R(T) = AT^n$ , with  $A/R = 0.014 \text{ K}^{-2.57}$ ,  $n = 2.57$ ; b) magnetic heat capacity contribution,  $C_m(T, H)$ , and high-temperature dependence,  $C_m/R(T, H = 0) = DT^{-2}$ , with  $D/R = 0.26 \text{ K}^2$ ; c) temperature dependence of the magnetic entropy change,  $-\Delta S_m$ , obtained from the  $C_m(T)$  data for the indicated magnetic field changes  $\Delta B$  (left axis, units in R; right axis, units in  $\text{mJ cm}^{-3} \text{ K}^{-1}$ ). The dashed line represents the full entropy content for the **mCB-8RE** containing 8 RE ions; d) temperature dependence of the adiabatic temperature change  $\Delta T_{\text{ad}}(T)$  for different field changes  $\Delta B$ .

available for covalent interactions. Thus, in contrast to transition metals, covalence plays a minor role in RE-ligand bonds and the nature of the coordination sphere is controlled by a tenuous balance between Coulombic interaction and steric hindrance.<sup>[97]</sup> Due to their high charge density, RE cations behave as hard Pearson acids and bind strongly with hard bases such as oxygen, and there is a linear relationship between the basicity of the carboxylates and the stability of the RE carboxylates.<sup>[104]</sup> Aromatic acids are among the most widely used to prepare such derivatives.<sup>[104,105]</sup> The aromatic fragments are rigid and facilitate the formation of ordered single crystals.<sup>[106]</sup> As mentioned in the introduction, icosahedral *closo*-carborane clusters are bulkier and more electron-withdrawing than a phenyl ring. The experimentally observed higher acidity of carboxylic acids of carboranes results in a lower basicity of the corresponding carboxylates, as compared with the benzoate anion. Thus, a combination of the weaker basicity and bulkier nature of the *closo*-carboranyl carboxylate derivatives may explain the observed SBUs and longer metal-to-metal distances of our rod-shaped units (elongation effect) when compared with conventional flat aromatic carboxylates. On one hand, the intermolecular interaction (e.g.,  $\pi$ - $\pi$  and/or C-H- $\pi$ ) between aromatic rings of aromatic carboxylates in the vicinity of a polymeric structure will not be present when replacing the aromatic rings by the aromatic 3D *closo*-carborane moieties. This can certainly increase the distances of the carboxylates in the rod-shaped structures and therefore the metal-metal distances. In addition, a somewhat weaker basicity of the carboranyl carboxylates could provide a looser bonding to the

RE cations than the corresponding phenyl carboxylates. All these carborane features could provide more flexibility to the linkers to accommodate different size RE cations in a linear rod-shaped SBU.

In order to test the above hypothesis, we have synthesized and characterized a  $\text{Ce}^{3+}$  MOF with the *m*-terphenyl-4,4-dicarboxylic acid (TPDC) ligand, which is the result of replacing the carborane fragment in *mCB-L* by a phenyl ring (Figure 5). Although the 3D structure of TPDC-Ce (Figure S10, Supporting Information) is different to that of our *mCB-Ce* one, it also consists of rod-shaped  $\text{LnO}_9$  polyhedra providing the  $[(\text{Ce})_2(\text{COO})_6(\text{O}_{\text{DMF}})]$  SBU (Figure 5a). Contrary to *mCB-Ce*, no nitrate anions from the starting Ce salt are incorporated in the TPDC-Ce structure. The absence of the nitrate anion in this new structure can be explained by the higher basicity of the TPDC-carboxylate, whereas a less basic *m*-carborane-carboxylate cannot substitute all nitrate anions from the starting  $\text{Ce}(\text{NO}_3)_2$ . Quite remarkably, the Ce-Ce distances in the flat aromatic MOF are significantly shorter than those found in the structure for *mCB-Ce* (4.137, 3.850 Å and 4.630, 4.720, 5.251 Å, respectively; See Table S2, Supporting Information, for full comparison of bonds and distances), and comparable to those observed in the RPF-4 family. Quite interestingly, whereas *mCB-L* carboxylates bond to the Ce atoms in a bridging mode (mostly type I in Figure 5c; Table S2, Supporting Information), those for the non-carborane carboxylate are all in a chelate bridging mode (III in Figure 5c). The higher number of chelate bridging mode coordination in the phenyl derivative result in shorter Ce...Ce distances. Conversely, the higher

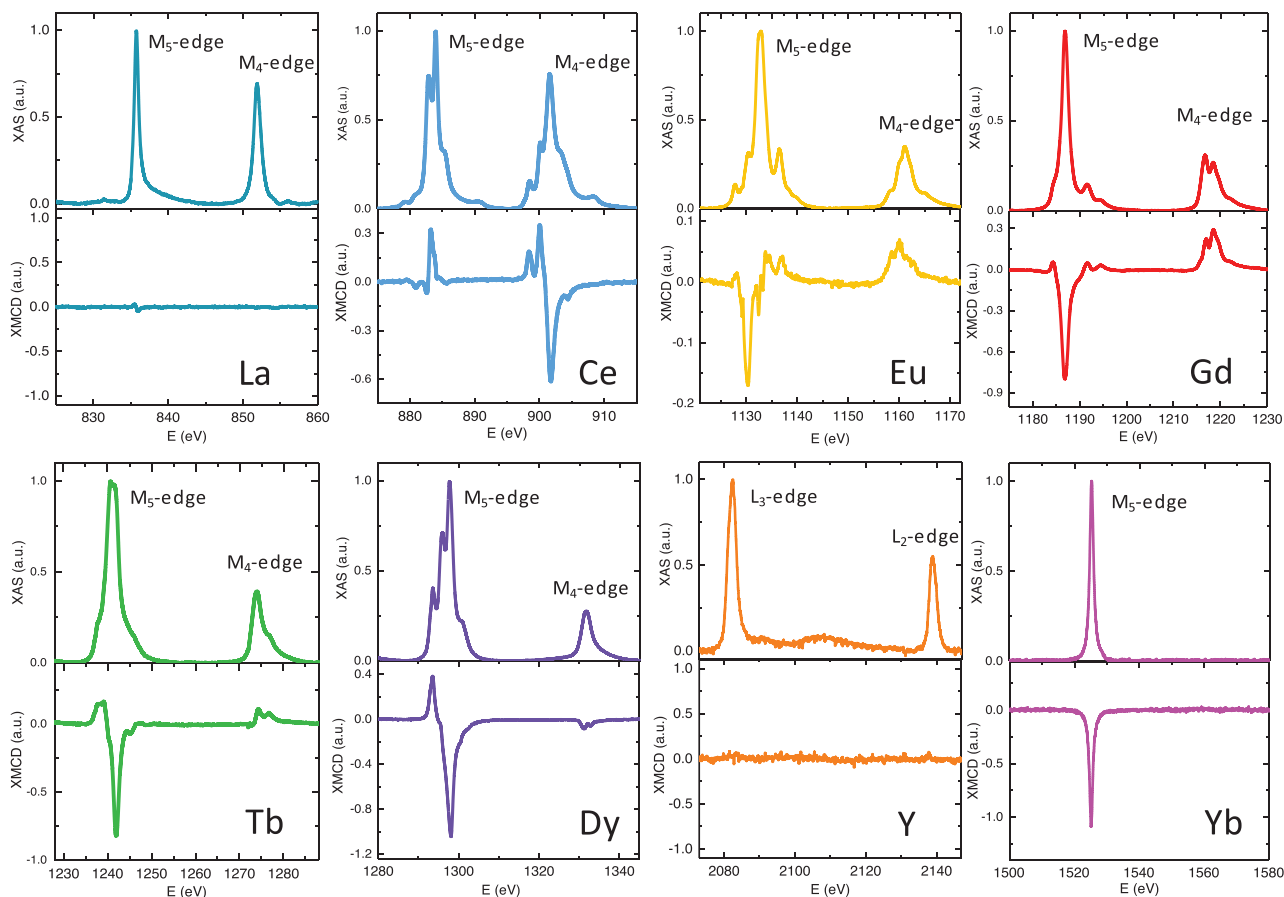


**Figure 9.** XAS and XMCD of *mCB-8RE*. Background-subtracted X-ray Absorption Spectroscopy (XAS), and X-Ray Magnetic Circular Dichroism (XMCD) spectra measured at 3.4 K and 6 T, at the  $L_{2,3}$  edge of Y, and  $M_{4,5}$  edges of La, Ce, Eu, Gd, Tb, Dy, and Yb. Spectra are displayed in order of decreasing ion size.

number of bridging mode coordination in the carborane derivative result in larger cations' distances. All these data suggest that the use of bulky linkers such as carboranes for the synthesis of multi-metal RE MTVMOFs directs the formation of SBUs with longer metal–metal distances, allowing the introduction of multiple cations with different size, and it may become a versatile tool for sequencing RE cations in this type of complex MOFs.

## 2.2. Optical Characterization

The absorption spectrum of *mCB-8RE* displays a slight broadening of the UV band in comparison to that for the free ligand *mCB-L* and similar to the Eu and Tb-MOFs (Figure S11, Supporting Information). The emission spectrum in the visible region for a powder sample of *mCB-8RE* ( $\lambda_{\text{ex}} = 280$  nm; air atmosphere; room temperature (RT)) is shown in Figure 6a. The spectrum shows the characteristic emission for  $\text{Eu}^{3+}$  (strongest peak at 614 nm) and  $\text{Tb}^{3+}$  (strongest peak at 543 nm). The first triplet state (T1) energy for *mCB-L*, calculated by time-dependent density functional theory (TDDFT), showed that our carborane linker is a good sensitizer for these two cations.<sup>[64]</sup> Overall the *mCB-8RE* shows a yellow-orange emission, with a 1931 CIE color

coordinate (0.40, 0.48). The emitted color is due to the combination of the two extreme colors (green and red) for the individual  $\text{Tb}^{3+}$  and  $\text{Eu}^{3+}$  lanthanides, respectively (Figure 6b). The luminescence decay curves for *mCB-8RE* (Figure S12, Supporting Information) exhibit the typical monoexponential decay functions with calculated lifetimes (850.8 and 741.9  $\mu\text{s}$  for the 543 and 614 nm bands, respectively) which are nearly identical to those of the individual *mCB-Tb* (849.7  $\mu\text{s}$ ) and *mCB-Eu* (739.0  $\mu\text{s}$ ) MOFs.<sup>[64]</sup> Thus, the luminescence properties of  $\text{Tb}^{3+}$  and  $\text{Eu}^{3+}$  are additive in *mCB-8RE*. The increased dilution of these two cations within the material prevents the energy transfer that was observed in the Eu/Tb binary MOFs.<sup>[64]</sup>

## 2.3. Static Magnetic Characterization

Figure 7a shows the magnetization of *mCB-8RE* as a function of the applied field,  $M(H)$ , measured at different temperatures between  $T = 1.8$  and 30 K. The magnetization of *mCB-8RE* at 1.8 K reaches 7.1  $\mu_{\text{B}}/\text{f.u.}$  at the maximum field applied (6 T), without reaching saturation. The temperature dependence of the susceptibility, plotted as  $\chi T(T)$  is shown in Figure 7b. The  $\chi T$  data tends at 190 K to the expected constant value of 13.9  $\text{emu.K mol}^{-1}$  calculated considering the contribution of  $\text{Tb}^{3+}$ ,  $\text{Dy}^{3+}$ ,  $\text{Gd}^{3+}$ ,  $\text{Tb}^{3+}$ ,



**Table 1.** Number of holes ( $n_h$ ), orbital ( $m_L$ ), spin ( $m_S$ ) and total ( $m_{TOT} = m_L + m_S$ ) magnetic moment per ion calculated from the sum rules at  $T = 3.4$  K and  $\mu_0 H = 6$  T.

RE	$n_h$	$m_L$ [ $\mu_B$ ]	$m_S$ [ $\mu_B$ ]	$m_{TOT}$ [ $\mu_B$ ]
Dy <sup>3+</sup>	5	2.37	2.09	4.46 ± 0.05
Tb <sup>3+</sup>	6	0.82	3.28	4.09 ± 0.08
Yb <sup>3+</sup>	1	0.95	0.38	1.26 ± 0.21
Ce <sup>3+</sup>	13	1.23	-0.42	0.81 ± 0.09
Gd <sup>3+</sup>	7	0.81	5.84	6.65 ± 0.05
Eu <sup>2+</sup> /Eu <sup>3+</sup> (0.2/0.8)	7.8	0.01	2.13	2.14 ± 0.35

Ce<sup>3+</sup>, and Eu<sup>2+</sup> ions, with the ion proportions given by ICP, and the Ce<sup>3+</sup>/Ce and Eu<sup>2+</sup>/Eu ratios obtained from XAS-XMCD measurements (vide infra). The theoretical contribution to the saturation of each ion, given by  $\chi T_{free\ ion} = g_j^2 J(J+1)/8$  (where  $g_j$  is the Landé constant and  $J$  the total angular momentum), is 11.8 for Tb<sup>3+</sup>, 14.1 for Dy<sup>3+</sup>, 7.9 for Gd<sup>3+</sup>, 2.6 for Yb<sup>3+</sup>, 0.8 for Ce<sup>3+</sup> and 7.9 emu K mol<sup>-1</sup> for Eu<sup>2+</sup>. Above this temperature, the  $\chi T(T)$  curve increases more abruptly owing to the non-saturated linear contribution of Eu<sup>3+</sup> ions, reaching a maximum value of 15.2 emu K mol<sup>-1</sup> at 300 K. This limit is close to the expected value, estimated considering the Eu<sup>3+</sup>/Eu ratio of ions present in the sample and their temperature-dependent contribution, which is also at the origin of the deviation from the linear behavior in the  $1/\chi$  data at high temperatures (see Figure 7b, inset). By decreasing the temperature, the  $\chi T$  value decreases smoothly till reaching 10.8 emu K mol<sup>-1</sup> at 2 K. Unlike in the mono-metallic Tb and Dy MOFs,<sup>[107]</sup> the  $\chi T(T)$  in **mCB-8RE** does not show an abrupt increase at low temperatures, indicating that the ferromagnetic interactions that were present in the former are diluted in the RE MTV MOF.

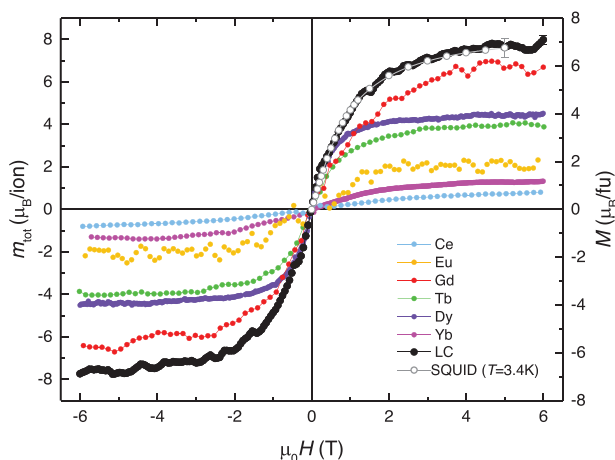


**Figure 10.**  $M(H)$  of **mCB-8RE** and ion contributions measured by XMCD( $H$ ). (Left scale) Data in color:  $m_{TOT}(H)/ion$  cycles measured for Dy, Tb, Gd, Ce, Yb, and Eu ions; (Right scale) Black bold symbols: magnetic moment for **mCB-8RE** calculated as the linear combination (LC) of the previous cycles, considering the elemental composition per formula unit. Open symbols:  $M(H)$  measured by SQUID at 3.4 K. The error bar accounts for the uncertainty in the molecular weight,  $M_w$  ( $\pm 1$  DMF of solvent per f.u.).

## 2.4. Heat Capacity and Magnetocaloric Effect

We have performed heat capacity (HC) measurements to characterize the thermal and magnetocaloric properties of our multi-metallic MOF material. We measured the heat capacity of **mCB-8RE** as a function of the temperature in the range 0.3–300 K and at different applied magnetic fields,  $\mu_0 H = 0, 0.5, 1, 2,$  and  $3$  T. **Figure 8a** shows the low-temperature region of the measured  $C(T)$  curves. The magnetic contribution to the heat capacitance,  $C_m(T)$  was obtained after subtracting the lattice contribution, which follows a power-law dependence,  $C_L = AT^n$  (**Figure 8b**). The  $C_m(T)$  curves exhibit a broad Schottky anomaly, which is shifted toward higher temperatures with increasing field. The magnetocaloric effect (MCE) performance parameters of the **mCB-8RE** material were determined from the HC data, following the procedure described elsewhere.<sup>[108]</sup> **Figure 8c** presents the magnetic entropy change  $\Delta S_m(T, \Delta B)$  obtained for selected changes of the magnetic field  $\Delta B = \mu_0(H_f - H_i)$ , where  $\mu_0 H_f = 0.5, 1, 2, 3$  T and  $\mu_0 H_i = 0$ . To facilitate comparison with existing literature, we discuss the results obtained for  $\mu_0 H_f = 2$  T, which is considered the standard as it can be easily attained with permanent magnets in magnetic refrigerator applications. For  $\Delta B = 2$  T the maximum entropy change value ( $-\Delta S_m^{max} = 7.34$  mJ cm<sup>-3</sup> K<sup>-1</sup>) is observed at  $T^{max} = 0.71$  K (**Figure 8c**, green curve). The full width at half maximum of the  $-\Delta S_m$  curve is  $\delta T_{FWHM} = 3.0$  K, and the relative cooling power is  $RCP = -\Delta S_m^{max} \times \delta T_{FWHM} = 22.0$  mJ cm<sup>-3</sup>. Besides, the adiabatic temperature change  $\Delta T_{ad}(T) = T_f - T_i$  obtained from the HC data is shown in **Figure 7d**. For  $\Delta B = 2$  T the maximum temperature decrease is  $\Delta T_{ad}^{max} = 5.05$  K at  $T = 0.76$  K (**Figure 8d**, green curve). Although these figures of merit are lower than those obtained for denser mono-metallic Gd compounds proposed as refrigerants at cryogenic temperatures,<sup>[108,109]</sup> the multi-metallic approach offers the possibility of combining Gd<sup>3+</sup> ion (favorable for MCE effect) with other lanthanides to obtain self-refrigerated multifunctional compounds for different applications, for example, {Gd-Dy} SMM units, {Gd-Tb}, {Gd-Er} qubits, {Gd-Eu/Tb}, {Gd-Tb-Eu} luminescent units, etc. We are currently working in this direction.

## 2.5. X-ray Absorption Spectroscopy and X-ray Magnetic Circular Dichroism

Element selective X-ray absorption spectroscopy (XAS) and X-ray magnetic circular dichroism (XMCD) experiments were performed to investigate the magnetism of each of the individual ions within the structure of the **mCB-8RE** material. **Figure 9** summarizes the XAS and XMCD spectra measured at a magnetic field of 6 T and 3.4 K at the  $L_{2,3}$  edge of Y and the  $M_{4,5}$  edges of La, Ce, Eu, Gd, Tb, Dy, and Yb. Spectra are displayed in order of decreasing ion size.

For yttrium, the XAS spectrum exhibits two peaks at the  $L_3$  (2082.4 eV) and  $L_2$  (2138.8 eV) edges expected for Y<sup>3+</sup> ion, and the XMCD signal is zero. Likewise, the XAS spectrum of lanthanum presents two peaks at the predicted positions for La<sup>3+</sup> ion at the  $M_5$  (835.7 eV) and  $M_4$  (851.8 eV) edges and, as in the case of Y, there is no dichroic signal. Thus, Y and La ions do not contribute to the overall magnetization of the sample.

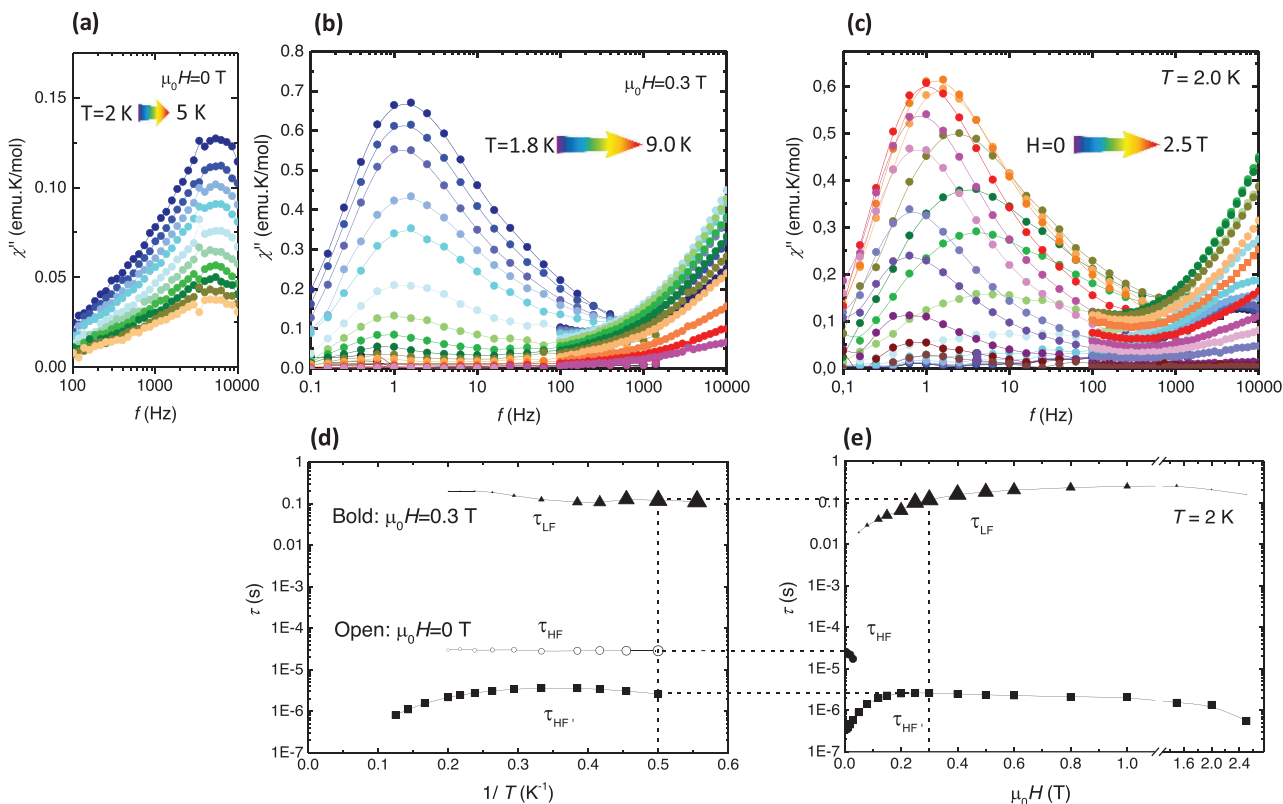


**Figure 11.** AC susceptibility. Top: out-of-phase  $\chi''(f)$  components of the susceptibility as a function of the frequency measured at a)  $\mu_0 H = 0$  T and b)  $\mu_0 H = 0.3$  T at different temperatures, and c) at  $T = 2.0$  K and different applied magnetic fields. Bottom: dependence of the relaxation time with d) the inverse temperature and e) with the applied magnetic field.

For gadolinium, the XAS at the  $M_5$  edge presents a pre-peak shoulder 1184.4 eV, main peak at 1186.8 and two satellites at 1191.5 and 1194.2 eV, whereas the  $M_4$  edge exhibits two peaks at 1216.6, 1218.4 eV. These spectral features show that Gd ion is in the common trivalent state.<sup>[110]</sup> In the case of terbium, the XAS spectra is related to the transition from  $3d^{10}4f^{8}$  to  $3d^9 4f^9$ . The  $3d - 4f$  absorption is characterized by a  $M_5$  with double-peak structure (1240.7, 1241.5 eV) and  $M_4$  at 1273.9 eV, clearly separated in energy. The XMCD signal is strong, as expected for a lanthanide having a high spin magnetic moment ( $J = 6$  for  $Tb^{3+}$ ). The high intensity of the XMCD at the  $M_5$  edge compared to the  $M_4$  edge indicates a strong contribution from the orbital moment of the Tb ion.<sup>[111]</sup> The XAS and XMCD line shapes resemble those earlier reported for  $Tb^{3+}$  at the  $M_{4,5}$  edge in different materials.<sup>[112–114]</sup> The absorption spectrum of dysprosium at the  $M_5$  edge exhibits a three-peak structure (1293.6, 1296.0, 1297.7 eV) and a single peak at the  $M_4$  edge (1331.7 eV). The XMCD has strong intensity at the position of the main  $M_5$  peak. The XAS and XMCD spectra correspond to Dy ion in trivalent state, as measured in other systems.<sup>[114,115]</sup> In ytterbium the XAS consists of a sharp, structureless peak at the  $M_5$  edge (1522.7 eV), due to the only allowed dipolar electronic  $3d^{10}4f_{7/2}^{13}$  to  $3d_{5/2}^9 4f_{7/2}^{14}$  transition, and the corresponding XMCD is a symmetric single-peak as expected for  $Yb^{3+}$ .<sup>[116]</sup>

XAS and XMCD results for Ce and Eu deserve special attention, as they show the coexistence of valence states. For cerium,

the spectral features of the XAS across the  $M_{4,5}$  edges reveal the presence of  $Ce^{3+}$  and a minor fraction of  $Ce^{4+}$ . By comparing the data against the experimental XAS of pure  $Ce_2O_3$  ( $Ce^{3+}$ ) and  $CeO_2$  ( $Ce^{4+}$ ) from reference,<sup>[117]</sup> we were able to quantify the fraction of  $Ce^{3+}$ - $Ce^{4+}$  to be 80%–20% (see Figure S14, Supporting Information). The XMCD arises mainly from the  $Ce^{3+}$  contribution, as observed in other systems with mixed  $Ce^{3+}/Ce^{4+}$  valence states.<sup>[118]</sup> In the case of europium, the XAS-XMCD spectra at the  $M_{4,5}$  edges evidence also the coexistence of two valence states,  $Eu^{3+}$  and  $Eu^{2+}$ . The experimental spectral characteristics could be explained considering a linear combination of the XAS-XMCD spectra calculated using atomic multiplet theory for magnetic  $Eu^{2+}(f^7, J = 7/2)$ ,  $Eu^{3+}(f^6, J = 1)$ , and non-magnetic  $Eu^{3+}(f^6, J = 0)$ , with weight percentages of 20%–20%–60%, respectively (see Figure S16, Supporting Information). The coexistence of  $Eu^{2+}/Eu^{3+}$  or  $Ce^{3+}/Ce^{4+}$  ions were already found in the  $Eu(NO_3)_3$  or  $Ce(NO_3)_3$  salt precursors, respectively, and the synthesized **mCB-8RE**, as confirmed by XPS (See Figures S13 and S14, Supporting Information).

The orbital moment ( $m_l$ ), spin moment ( $m_s$ ) and total magnetic moment ( $m_{TOT} = m_l + m_s$ ) for  $Dy^{3+}$ ,  $Tb^{3+}$ ,  $Yb^{3+}$ ,  $Ce^{3+}$ , and  $Gd^{3+}$  ions were determined from the XAS-XMCD spectra across the  $M_{4,5}$  edges using the corrected sum rules for lanthanides,<sup>[111,119]</sup> following the procedure described by Tripathi<sup>[120]</sup> (see Supporting Information S4 for details). The correction is needed to take into account the large jj mixing between

the  $3d^{5/2}$  and  $3d^{3/2}$  core levels, on the one hand, and the contribution of the  $\langle T_z \rangle$  magnetic dipole term, which is not negligible for  $RE^{3+}$  ions, on the other. To obtain the magnetic moment of Cerium from the sum rules, the  $Ce^{3+}$  XAS was separated out by subtracting the  $Ce^{4+}$  contribution (see Section 3). In the case of Europium, the dichroic signal mainly arises from the  $Eu^{2+}$  ions, for which the  $\langle T_z \rangle \approx 0$ ,<sup>[121]</sup> and has a contribution from the  $Eu^{3+}$  ( $f^6$ ,  $J = 1$ ) fraction of ions, whereas the absorption spectrum is owed to all Eu ions in the sample. Hence, the “averaged” magnetic moment per Eu ion was calculated applying the sum rules with  $n_h = 7.8$ , taking into account the experimentally determined fraction of ions,  $Eu^{2+}(Eu^{3+}) = 0.2(0.8)$ , and the number of holes of each one,  $n_h = 7$  ( $Eu^{2+}$ ), 8 ( $Eu^{3+}$ ). Table 1 summarizes the obtained orbital, spin and total magnetic moments for all RE magnetic ions in **mCB-8RE**.

The field-dependence of the dichroic signal, XMCD( $H$ ), was independently measured for Gd, Tb, Dy, Yb, and Eu by following the intensity of the XMCD peak at the  $M_5$  edge (the  $M_4$  edge for Ce), between  $-6$  T and  $6$  T (Figure 10). The  $m_{TOT}(H)$  curve for each ion was found scaling the XMCD( $H$ ) with the value found from the sum rules at  $6$  T. The total magnetic moment per formula unit of the **mCB-8RE** compound was obtained considering the element composition per formula unit and the magnetic moment determined for each ion as:

$$m_{mCB-8RE}(\mu_B/fu) = (Ce/fu) \times (Ce^{3+}/Ce^{4+}) \times m_{Ce3+} + (Gd^{3+}/fu) \times m_{Gd3+} + (Tb^{3+}/fu) \times m_{Tb3+} + (Dy^{3+}/fu) \times m_{Dy3+} + (Yb^{3+}/fu) \times m_{Yb3+} + (Eu/fu) \times m_{Eu} \quad (1)$$

Figure 10 shows that the field-dependence  $m_{mCB-8RE}(H)$  determined from the linear combination of elemental  $m_{TOT}(H)$  curves is in very good agreement with the magnetization curve  $M(H)$  measured by SQUID for **mCB-8RE** at  $T = 3.4$  K, within experimental error.

Additional XAS-XMCD measurements were conducted at a higher temperature of  $T \approx 21$  K (see Supporting Information, section 5), which revealed qualitatively similar spectral characteristics (Figure S17, Supporting Information). The obtained  $m_{TOT}(H)$  curves at this temperature were obviously noisier, and showed a more rounded, quasi-linear behavior, as expected for RE paramagnetic ions. However, their weighted linear combination was again in good agreement with the magnetization curve of the compound determined by SQUID at  $21$  K (Figure S18, Supporting Information). Moreover, the  $\chi T$  values obtained through XMCD at  $3.4$  and  $21$  K (using the initial  $M/H$  slope as  $\chi$ ) were also consistent with the SQUID-determined-values at  $0.1$  T (Figure 6b, star symbols).

The above analysis of **mCB-8RE** is a beautiful example showing the power of element-selective XMCD technique to investigate the magnetic response of individual ions within a very complex material. In previous works in the literature, XMCD was used to study the magnetism of 2 or 3 three ions in intermetallics,<sup>[122,123]</sup>  $3d-4f$ <sup>[124,125]</sup> or  $4f-4f$ <sup>[126]</sup> clusters. In this work, it was possible to determine the spectroscopic and magnetic properties of up to eight different RE ions in **mCB-8RE**.

## 2.6. Dynamic Spin Magnetic Relaxation

AC susceptibility experiments as a function of the frequency, magnetic field and temperature were performed to investigate the spin magnetic relaxation properties of the **mCB-8RE** material (Figure 11). At zero applied field, the out-of-phase component of the susceptibility measured at different temperatures shows no frequency dependence (Figure 11a). The relaxation time as a function of the inverse temperature,  $\tau(1/T)$ , determined from the  $\chi''(f)$  peak is  $\tau_{HF} \approx 3 \times 10^{-5}$  s, and corresponds to a mechanism of spin relaxation through Quantum Tunneling of the Magnetization (QTM). Under the application of a constant magnetic field,  $\mu_0 H = 0.3$  T, the  $\chi''(f, T)$  curves exhibit a peak at very low frequencies and a tail at higher frequencies (Figure 11b). The relaxation time as a function of the temperature for this second process was estimated as:<sup>[42]</sup>

$$\tau(T) = \frac{\chi''}{2\pi f (\chi' - \chi_s)} \quad (2)$$

where  $\chi_s$  is the adiabatic susceptibility (i.e., in the limit of  $f \rightarrow \infty$ ), which was approximated to  $\chi_s \approx 0$ . The determined  $\tau(1/T, 0.3$  T) dependence (Figure 11d) reflects the existence of a thermally-activated spin relaxation mechanism at higher temperatures (although the energy barrier cannot be accurately determined from the existing data) which is replaced by QTM with  $\tau_{HF} \approx 3.6 \times 10^{-6}$  s at low temperatures, and a very slow relaxation mechanism with  $\tau_{LF} \approx 0.12$  s associated to a direct process, affected by bottleneck. This later type of process has been often observed in lanthanide-based coordination polymers.<sup>[46,127]</sup> The  $\chi''(f, H)$  measurements at constant  $T = 2$  K shown in Figure 11c allowed to determine the magnetic field dependence of the relaxation time,  $\tau(H)$ , for the three observed processes Figure 11e, and confirm the assigned relaxation mechanisms.

## 3. Conclusions

This multidisciplinary study reveals that designing rare-earth (RE) MOFs with 3D bulky carborane-based linkers offers a unique opportunity to achieve highly multi-metal RE multivariate (MTV) MOFs. With the present method, scientists can select, based on intuition, calculations or machine learning methods, the desired combination of metals and their ratio for a potential property or combination of various. A proof of concept is provided with the MTV MOF (**mCB-8RE**), the first-ever MOF structure that incorporates eight different sizes of RE cations (La, Ce, Eu, Gd, Tb, Dy, Y, and Yb) that are homogeneously distributed in the MOF network. This design strategy has been further validated by the synthesis of the corresponding MTV MOFs containing two (La and Yb, or Ce and Yb), four (La, Ce, Gd, and Yb) or six (La, Ce, Gd, Tb, Y, and Yb) RE cations in equimolar amounts. The comparison of the mono- and multi-metallic RE MOF structures with a cerium(III) TPDC structure, where the 3D purely inorganic carborane moiety has been replaced by a 2D phenyl group, and with the RPF-4 family, provides solid evidence for the role of the carborane linker in the achievement of these new family of RE MTV MOFs. We demonstrate the co-existence of the eight RE metals in **mCB-8RE**, and showcase the potentially tunable functionalities provided by the RE cations. Those



provide optical, magnetocaloric and magnetic properties to the new **mCB-8RE** material. The foregoing results show, for example, an interesting magnetocaloric effect (MCE) that would permit preparing self-refrigerated {Gd-nRE} materials for different applications (e.g., SMM memories, qubits, luminescent units etc), and revealed that **mCB-8RE** exhibits Quantum Tunneling of the Magnetization (QTM) under  $H = 0$  and field-induced slow relaxation of the magnetization through, simultaneously, a thermally-activated mechanism and a direct mechanism.

This work paves the way for the synthesis of MTV MOFs with different combinations and ratios of RE cations, for fundamental research and the development of multifunctional materials with customized magnetic, optical and thermal properties. We highlight that our strategy for the preparation of MTV materials could be used to develop “QuMOFs” with high dimensionality of qubits (either MOFs with large number of qubits, or d-state Qudits, making use of the three different coordination sites present in the SBU), to advance in the scaling of molecular systems for Quantum Computing, a very attractive possibility that we are prospecting now.

## Supporting Information

Supporting Information is available from the Wiley Online Library or from the author.

## Acknowledgements

This work was financially supported by MINECO (PID2019-106832RB-I00, PID2021-123287OB-I00), MICINN through the Severo Ochoa Program for Centers of Excellence for the FUNFUTURE (SEV-2017-0706 projects), the Generalitat de Catalunya (2021/SGR/00442), and the Aragonese Project RASMIA E12-23R. Zhen Li and Xiao-Bao Li acknowledge the China Scholarship Council (CSC) for their PhD grants (201808310071 and 202106650003, respectively). Xiao-Bao Li is enrolled in the UAB Ph.D. program. XAS and XMCD experiments were performed at the BOREAS beamline of the ALBA Synchrotron Light Source via official proposal 2022085925 and in-house beamtime.

## Conflict of Interest

The authors declare no conflict of interest.

## Author Contributions

J.G.P. conceived the project concept. J.G.P., E. B., and Z.L. designed the detailed project scope and the experiments. Z.L. performed the sample preparation and conducted sample optical measurements under the supervision of C. R. and D. R. Z.L. conducted basic characterizations. X-B. L. performed the sample preparation and characterization for the 2, 4, and 6 RE MOFs. M.E.L. conducted the X-ray diffraction measurements. A.A., M.V., and E.B. conducted the thermal and magnetic measurements. A. E. C. conducted the SEM-EDX measurements. J.G.P., E. B., and Z.L. analyzed the data and wrote the paper. A.A., C. R., F.T., C.V., and F.G. discussed the results and commented on the manuscript. All authors revised the manuscript.

## Data Availability Statement

The data that support the findings of this study are available in the supplementary material of this article.

## Keywords

carboranes, lanthanide molecular magnets, multivariate metal-organic frameworks, rare-earth materials

Received: June 28, 2023

Published online:

- [1] J.-W. Yeh, S.-K. Chen, S.-J. Lin, J.-Y. Gan, T.-S. Chin, T.-T. Shun, C.-H. Tsau, S.-Y. Chang, *Adv. Eng. Mater.* **2004**, *6*, 299.
- [2] B. Cantor, I. T. H. Chang, P. Knight, A. J. B. Vincent, *Mater. Sci. Eng., A* **2004**, *375–377*, 213.
- [3] A. Amiri, R. Shahbazian-Yassar, *J. Mater. Chem. A* **2021**, *9*, 782.
- [4] E. P. George, D. Raabe, R. O. Ritchie, *Nat. Rev. Mater.* **2019**, *4*, 515.
- [5] J. Castells-Gil, N. Almora-Barrios, B. Lerma-Berlanga, N. M. Padial, C. Martí-Gastaldo, *Chem. Sci.* **2023**, *14*, 6826.
- [6] C.-B. Celia, V. A. de la Pena-O’Shea, I. Puente-Orench, J. R. de Paz, R. Saez-Puche, E. Gutierrez-Puebla, F. Gandara, A. Monge, *Sci. Adv.* **2022**, *3*, e1700773.
- [7] C. López-García, S. Canossa, J. Hadermann, G. Gorni, F. E. Oropeza, V. A. De La Peña O’Shea, M. Iglesias, M. A. Monge, E. Gutiérrez-Puebla, F. Gándara, *J. Am. Chem. Soc.* **2022**, *144*, 16262.
- [8] M. Y. Masoomi, A. Morsali, A. Dhakshinamoorthy, H. Garcia, *Angew. Chem., Int. Ed.* **2019**, *58*, 15188.
- [9] S. Abednatanzi, P. G. Derakhshandeh, H. Depauw, F.-X. Coudert, H. Vrielinck, P. Van Der Voort, K. Leus, *Chem. Soc. Rev.* **2019**, *48*, 2535.
- [10] C. Castillo-Blas, F. Gándara, *Isr. J. Chem.* **2018**, *58*, 1036.
- [11] H. Furukawa, U. Müller, O. M. Yaghi, *Angew. Chem., Int. Ed.* **2015**, *54*, 3417.
- [12] W. Xu, B. Tu, Q. Liu, Y. Shu, C.-C. Liang, C. S. Diercks, O. M. Yaghi, Y.-B. Zhang, H. Deng, Q. Li, *Nat. Rev. Mater.* **2020**, *5*, 764.
- [13] S. Patil, P. Raizada, V. Hasija, P. Singh, V. K. Thakur, V.-H. Nguyen, *Mater. Today Energy* **2021**, *19*, 100589.
- [14] M. Zhang, W. Xu, T. Li, H. Zhu, Y. Zheng, *Inorg. Chem.* **2020**, *59*, 15467.
- [15] Y. Wang, Y.-Y. Xue, L.-T. Yan, H.-P. Li, Y.-P. Li, E.-H. Yuan, M. Li, S.-N. Li, Q.-G. Zhai, *ACS Appl. Mater. Interfaces* **2020**, *12*, 24786.
- [16] M. Giménez-Marqués, A. Santiago-Portillo, S. Navalón, M. Álvaro, V. Briois, F. Nouar, H. Garcia, C. Serre, *J. Mater. Chem. A* **2019**, *7*, 20285.
- [17] E. López-Maya, N. M. Padial, J. Castells-Gil, C. R. Ganivet, A. Rubio-Gaspar, F. G. Cirujano, N. Almora-Barrios, S. Tatay, S. Navalón, C. Martí-Gastaldo, *Angew. Chem., Int. Ed.* **2021**, *60*, 11868.
- [18] J. I. Deneff, K. S. Butler, L. E. S. Rohwer, C. J. Pearce, N. R. Valdez, M. A. Rodriguez, T. S. Luk, D. F. Sava Gallis, *Angew. Chem., Int. Ed.* **2021**, *60*, 1203.
- [19] K. A. White, D. A. Chengelis, K. A. Gogick, J. Stehman, N. L. Rosi, S. Petoud, *J. Am. Chem. Soc.* **2009**, *131*, 18069.
- [20] R. Rajak, R. Kumar, S. N. Ansari, M. Saraf, S. M. Mobin, *Dalton Trans.* **2020**, *49*, 11792.
- [21] K. M. Choi, H. M. Jeong, J. H. Park, Y.-B. Zhang, J. K. Kang, O. M. Yaghi, *ACS Nano* **2014**, *8*, 7451.
- [22] N. Hanikel, X. Pei, S. Chheda, H. Lyu, W. Jeong, J. Sauer, L. Gagliardi, O. M. Yaghi, *Science (80-)* **2021**, *374*, 454.
- [23] L. J. Wang, H. Deng, H. Furukawa, F. Gándara, K. E. Cordova, D. Peri, O. M. Yaghi, *Inorg. Chem.* **2014**, *53*, 5881.
- [24] C. Castillo-Blas, N. López-Salas, M. C. Gutiérrez, I. Puente-Orench, E. Gutiérrez-Puebla, M. L. Ferrer, M. Á. Monge, F. Gándara, *J. Am. Chem. Soc.* **2019**, *141*, 1766.
- [25] X. Zhao, Z. Xue, W. Chen, X. Bai, R. Shi, T. Mu, *J. Mater. Chem. A* **2019**, *7*, 26238.

- [26] C. López-García, S. Canossa, J. Hadermann, G. Gorni, F. E. Oropeza, V. A. De La Peña O'Shea, M. Iglesias, M. A. Monge, E. Gutiérrez-Puebla, F. Gándara, *J. Am. Chem. Soc.* **2022**, *144*, 16262.
- [27] W. Xu, H. Chen, K. Jie, Z. Yang, T. Li, S. Dai, *Angew. Chem., Int. Ed.* **2019**, *58*, 5018.
- [28] M. Viciano-Chumillas, X. Liu, A. Leyva-Pérez, D. Armentano, J. Ferrando-Soria, E. Pardo, *Coord. Chem. Rev.* **2022**, *451*, 214273.
- [29] Z. Ji, T. Li, O. M. Yaghi, *Science (80-)* **2020**, *369*, 674 LP.
- [30] S. Abednatanzi, P. G. Derakhshandeh, H. Depauw, F.-X. Coudert, H. Vrielinck, P. Van Der Voort, K. Leus, *Chem. Soc. Rev.* **2019**, *48*, 2535.
- [31] B. Zheng, J. Fan, B. Chen, X. Qin, J. Wang, F. Wang, R. Deng, X. Liu, *Chem. Rev.* **2022**, *122*, 5519.
- [32] X. Shi, B. Cao, J. Liu, J. Zhang, Y. Du, *Small* **2021**, *17*, 2005371.
- [33] Q. Zhang, Z. Gao, X. Shi, C. Zhang, K. Liu, J. Zhang, L. Zhou, C. Ma, Y. Du, *J. Rare Earths* **2021**, *39*, 1.
- [34] J. Wang, X. Sun, L. Xu, J. Xia, Y. Yang, Z. Yin, F. Luo, Y. Du, *Adv. Mater. Interfaces* **2020**, *7*, 1902168.
- [35] D. Zhou, D. Liu, G. Pan, X. Chen, D. Li, W. Xu, X. Bai, H. Song, *Adv. Mater.* **2017**, *29*, 1704149.
- [36] T. Zhang, X. Wu, Y. Fan, C. Shan, B. Wang, H. Xu, Y. Tang, *Chem-NanoMat* **2020**, *6*, 1119.
- [37] I. Norrbo, J. M. Carvalho, P. Laukkanen, J. Mäkelä, F. Mamedov, M. Peurla, H. Helminen, S. Pihlasalo, H. Härmä, J. Sinkkonen, M. Lastusaari, *Adv. Funct. Mater.* **2017**, *27*, 1606547.
- [38] Y. Xu, Z. Zeng, D. Zhang, S. Liu, X. Wang, S. Li, C. Cheng, J. Wang, Y. Liu, G. De, C. Zhang, W. Qin, Y. Du, *Adv. Opt. Mater.* **2020**, *8*, 1901495.
- [39] X. Gui, W. Xie, *Chem. Mater.* **2020**, *32*, 3922.
- [40] J.-C. G. Bünzli, C. Piguet, *Chem. Soc. Rev.* **2005**, *34*, 1048.
- [41] B. Sieklucka, D. Pinkowicz, *Molecular Magnetic Materials*, Wiley-VCH Verlag GmbH, Weinheim, Germany **2017**.
- [42] S. V. Eliseeva, J.-C. G. Bünzli, *Chem. Soc. Rev.* **2010**, *39*, 189.
- [43] D. Prodius, A.-V. Mudring, *Coord. Chem. Rev.* **2018**, *363*, 1.
- [44] R. Sessoli, A. K. Powell, *Coord. Chem. Rev.* **2009**, *253*, 2328.
- [45] R. A. Layfield, M. Murugesu, *Lanthanides and actinides in Molecular magnetism*, Wiley-VCH, Weinheim, Germany **2015**.
- [46] E. Bartolomé, A. Arauzo, J. Luzón, J. Bartolomé, F. Bartolomé, in *Handbook of Magnetic Materials* (Ed.: E. Brück), Elsevier, San Diego **2017**.
- [47] O. Guillou, C. Daiguebonne, G. Calvez, K. Bernot, *Acc. Chem. Res.* **2016**, *49*, 844.
- [48] A. Abdallah, S. Freslon, X. Fan, A. Rojo, C. Daiguebonne, Y. Suffren, K. Bernot, G. Calvez, T. Roisnel, O. Guillou, *Inorg. Chem.* **2019**, *58*, 462.
- [49] X. Rao, T. Song, J. Gao, Y. Cui, Y. Yang, C. Wu, B. Chen, G. Qian, *J. Am. Chem. Soc.* **2013**, *135*, 15559.
- [50] J. Zhou, Q. Liu, W. Feng, Y. Sun, F. Li, *Chem. Rev.* **2015**, *115*, 395.
- [51] S. Freslon, Y. Luo, C. Daiguebonne, G. Calvez, K. Bernot, O. Guillou, *Inorg. Chem.* **2016**, *55*, 794.
- [52] E. Bartolomé, J. Bartolomé, A. Arauzo, J. Luzón, R. Cases, S. Fuertes, V. Sicilia, A. I. Sánchez-Cano, J. Aporta, S. Melnic, D. Prodius, S. Shova, *J. Mater. Chem. C* **2018**, *6*, 5286.
- [53] I. Mamedov, T. N. Parac-Vogt, N. K. Logothetis, G. Angelovski, *Dalton Trans.* **2010**, *39*, 5721.
- [54] D. Aguilà, O. Roubeau, G. Aromí, *Dalton Trans.* **2021**, *50*, 12045.
- [55] G. Aromí, D. Aguilà, P. Gamez, F. Luis, O. Roubeau, *Chem. Soc. Rev.* **2012**, *41*, 537.
- [56] D. Aguilà, L. A. Barrios, V. Velasco, O. Roubeau, A. Repollés, P. J. Alonso, J. Sesé, S. J. Teat, F. Luis, G. Aromí, *J. Am. Chem. Soc.* **2014**, *136*, 14215.
- [57] J. J. Le Roy, J. Cremers, I. A. Thomlinson, M. Slota, W. K. Myers, P. H. Horton, S. J. Coles, H. L. Anderson, L. Bogani, *Chem. Sci.* **2018**, *9*, 8474.
- [58] V. Velasco, L. A. Barrios, M. Schütze, O. Roubeau, F. Luis, S. J. Teat, D. Aguilà, G. Aromí, *Chem. - Eur. J.* **2019**, *25*, 15228.
- [59] E. Macaluso, M. Rubín, D. Aguilà, A. Chiesa, L. A. Barrios, J. I. Martínez, P. J. Alonso, O. Roubeau, F. Luis, G. Aromí, S. Carretta, *Chem. Sci.* **2020**, *11*, 10337.
- [60] A. D. Burrows, *CrystEngComm* **2011**, *13*, 3623.
- [61] R. F. D'vries, S. Álvarez-García, N. Snejko, L. E. Bausá, E. Gutiérrez-Puebla, A. De Andrés, M. Á. Monge, *J. Mater. Chem. C* **2013**, *1*, 6316.
- [62] R. L. Vasile, A. A. Godoy, I. Puente Orench, N. M. Nemes, V. A. De La Peña O'Shea, E. Gutiérrez-Puebla, J. L. Martínez, M. Á. Monge, F. Gándara, *Chem. Mater.* **2022**, *34*, 7029.
- [63] A. Schoedel, M. Li, D. Li, M. O'keeffe, O. M. Yaghi, *Chem. Rev.* **2016**, *116*, 12466.
- [64] Z. Li, R. Núñez, M. E. Light, E. Ruiz, F. Teixidor, C. Viñas, D. Ruiz-Molina, C. Roscini, J. G. Planas, *Chem. Mater.* **2022**, *34*, 4795.
- [65] J. Poater, C. Viñas, I. Bennour, S. Escayola, M. Solà, F. Teixidor, *J. Am. Chem. Soc.* **2020**, *142*, 9396.
- [66] J. Poater, M. Solà, C. Viñas, F. Teixidor, *Angew. Chem., Int. Ed.* **2014**, *53*, 12191.
- [67] J. Poater, C. Viñas, M. Solà, F. Teixidor, *Nat. Commun.* **2022**, *13*, 3844.
- [68] J. Plešek, *Chem. Rev.* **1992**, *92*, 269.
- [69] M. Scholz, E. Hey-Hawkins, *Chem. Rev.* **2011**, *111*, 7035.
- [70] R. N. Grimes, *Carboranes*, Academic Press, New York **2016**.
- [71] F. Teixidor, D. E. Kaufmann, *Science of Synthesis: Houben-Weyl Methods of Molecular Transformations*, Georg Thieme Verlag, Stuttgart **2015**.
- [72] S. Fujii, *MedChemComm* **2016**, *7*, 1082.
- [73] F. Issa, M. Kassiou, L. M. Rendina, *Chem. Rev.* **2011**, *111*, 5701.
- [74] J. F. Valliant, K. J. Guenther, A. S. King, P. Morel, P. Schaffer, O. O. Sogbein, K. A. Stephenson, *Coord. Chem. Rev.* **2002**, *232*, 173.
- [75] O. K. Farha, A. M. Spokoyny, K. L. Mulfort, M. F. Hawthorne, C. A. Mirkin, J. T. Hupp, *J. Am. Chem. Soc.* **2007**, *129*, 12680.
- [76] Y.-S. Bae, O. K. Farha, A. M. Spokoyny, C. A. Mirkin, J. T. Hupp, R. Q. Snurr, *Chem. Commun.* **2008**, *4135*, 4135.
- [77] O. K. Farha, A. M. Spokoyny, K. L. Mulfort, S. Galli, J. T. Hupp, C. A. Mirkin, *Small* **2009**, *5*, 1727.
- [78] Y.-S. Bae, A. M. Spokoyny, O. K. Farha, R. Q. Snurr, J. T. Hupp, C. A. Mirkin, *Chem. Commun.* **2010**, *46*, 3478.
- [79] A. M. Spokoyny, O. K. Farha, K. L. Mulfort, J. T. Hupp, C. A. Mirkin, *Inorganica Chim Acta* **2010**, *364*, 266.
- [80] S.-L. Huang, Y.-J. Lin, W.-B. Yu, G.-X. Jin, *ChemPlusChem* **2012**, *77*, 141.
- [81] R. D. Kennedy, V. Krungleviciute, D. J. Clingerman, J. E. Mondloch, Y. Peng, C. E. Wilmer, A. A. Sarjeant, R. Q. Snurr, J. T. Hupp, T. Yildirim, O. K. Farha, C. A. Mirkin, *Chem. Mater.* **2013**, *25*, 3539.
- [82] D. J. Clingerman, W. Morris, J. E. Mondloch, R. D. Kennedy, A. A. Sarjeant, C. Stern, J. T. Hupp, O. K. Farha, C. A. Mirkin, *Chem. Commun.* **2015**, *51*, 6521.
- [83] Z. Li, D. Choquesillo-Lazarte, J. Fraile, C. Viñas, F. Teixidor, J. G. Planas, *Dalton Trans.* **2022**, *51*, 1137.
- [84] Z. Li, J. Fraile, C. Viñas, F. Teixidor, J. G. Planas, *Chem. Commun.* **2021**, *57*, 2523.
- [85] L. Gan, A. Chidambaram, P. G. Fonquernie, M. E. Light, D. Choquesillo-Lazarte, H. Huang, E. Solano, J. Fraile, C. Viñas, F. Teixidor, J. A. R. Navarro, K. C. Stylianou, J. G. Planas, *J. Am. Chem. Soc.* **2020**, *142*, 8299.
- [86] F. Tan, A. López-Periago, M. E. Light, J. Cirera, E. Ruiz, A. Borrás, F. Teixidor, C. Viñas, C. Domingo, J. G. Planas, *Adv. Mater.* **2018**, *30*, 1800726.
- [87] M. Y. Tsang, S. Rodríguez-Hermida, K. C. Stylianou, F. Tan, D. Negi, F. Teixidor, C. Viñas, D. Choquesillo-Lazarte, C. Verdugo-Escamilla, M. Guerrero, J. Sort, J. Juanhuix, D. Maspoch, J. Giner Planas, *Cryst. Growth Des.* **2017**, *17*, 846.

- [88] S. Rodríguez-Hermida, M. Y. Tsang, C. Vignatti, K. C. Stylianou, V. Guillermin, J. Pérez-Carvajal, F. Teixidor, C. Viñas, D. Choquesillo-Lazarte, C. Verdugo-Escamilla, I. Peral, J. Juanhuix, A. Verdaguer, I. Imaz, D. Maspoch, J. Giner Planas, *Angew. Chem., Int. Ed.* **2016**, *55*, 16049.
- [89] F. Teixidor, G. Barberà, A. Vaca, R. Kivekäs, R. Sillanpää, J. Oliva, C. Viñas, *J. Am. Chem. Soc.* **2005**, *127*, 10158.
- [90] F. Di Salvo, M. Y. Tsang, F. Teixidor, C. Viñas, J. G. Planas, J. Crassous, N. Vanthuyne, N. Aliaga-Alcalde, E. Ruiz, G. Coquerel, S. Clevers, V. Dupray, D. Choquesillo-Lazarte, M. E. Light, M. B. Hursthouse, *Chem. Eur. J.* **2014**, *20*, 1081.
- [91] J. Soldevila-Sanmartín, E. Ruiz, D. Choquesillo-Lazarte, M. E. Light, C. Vinas, F. Teixidor, R. Nunez, J. Pons, J. G. Planas, *J. Mater. Chem. C* **2021**, *9*, 7643.
- [92] L. Schwartz, L. Eriksson, R. Lomoth, F. Teixidor, C. Viñas, S. Ott, *Dalton Trans.* **2008**, 2379.
- [93] F. Teixidor, R. Núñez, C. Viñas, R. Sillanpää, R. Kivekäs, *Angew. Chem., Int. Ed.* **2000**, *39*, 4290.
- [94] R. Núñez, P. Farràs, F. Teixidor, C. Viñas, R. Sillanpää, R. Kivekäs, *Angew. Chem., Int. Ed.* **2006**, *45*, 1270.
- [95] K. Hermansson, M. Wójcik, S. Sjöberg, *Inorg. Chem.* **1999**, *38*, 6039.
- [96] F. Gándara, A. D. Andrés, B. Gómez-Lor, E. Gutiérrez-Puebla, M. Iglesias, M. A. Monge, D. M. Proserpio, N. Snejko, *Cryst. Growth Des.* **2008**, *8*, 378.
- [97] C. Huang, *Rare Earth Coordination Chemistry: Fundamentals and Applications*, Wiley, Hoboken, New Jersey **2010**.
- [98] D.-J. Kim, S.-H. Hyun, S.-G. Kim, M. Yashima, *J. Am. Ceram. Soc.* **1994**, *77*, 597.
- [99] Y. Han, X. Li, L. Li, C. Ma, Z. Shen, Y. Song, X. You, *Inorg. Chem.* **2010**, *49*, 10781.
- [100] W. Ding, L. Zhao, X. Yuan, L. Zhang, B. Chen, Q. Ju, Z. Fang, *J. Mater. Chem. C* **2020**, *8*, 3176.
- [101] L. Armelao, S. Quici, F. Barigelletti, G. Accorsi, G. Bottaro, M. Cavazzini, E. Tondello, *Coord. Chem. Rev.* **2010**, *254*, 487.
- [102] R. C. Shiery, J. L. Fulton, M. Balasubramanian, M.-T. Nguyen, J.-B. Lu, J. Li, R. Rousseau, V.-A. Glezakou, D. C. Cantu, *Inorg. Chem.* **2021**, *60*, 3117.
- [103] F. Saraci, V. Quezada-Novoa, P. R. Donnarumma, A. J. Howarth, *Chem. Soc. Rev.* **2020**, *49*, 7949.
- [104] R. Janicki, A. Mondry, P. Starynowicz, *Coord. Chem. Rev.* **2017**, *340*, 98.
- [105] V. V. Utochnikova, A. S. Kalyakina, N. N. Solodukhin, A. N. Aslandukov, *Eur. J. Inorg. Chem.* **2019**, *2019*, 2320.
- [106] A. Deluzet, W. Maudez, C. Daigebonne, O. Guillou, *Cryst. Growth Des.* **2003**, *3*, 475.
- [107] Manuscript in preparation.
- [108] G. Lorusso, J. W. Sharples, E. Palacios, O. Roubeau, E. K. Brechin, R. Sessoli, A. Rossin, F. Tuna, E. J. L. McInnes, D. Collison, M. Evangelisti, *Adv. Mater.* **2013**, *25*, 4653.
- [109] A. Arauzo, A. Lazarescu, S. Shova, E. Bartolomé, R. Cases, J. Luzón, J. Bartolomé, C. Turta, *Dalton Trans.* **2014**, *43*, 12342.
- [110] N. A. Anderson, M. Hupalo, D. Keavney, M. Tringides, D. Vaknin, *J. Magn. Magn. Mater.* **2019**, *474*, 666.
- [111] B. T. Thole, P. Carra, F. Sette, G. Van Der Laan, *Phys. Rev. Lett.* **1992**, *68*, 1943.
- [112] V. Cuartero, S. Lafuerza, G. Subías, J. García, E. Schierle, J. Blasco, J. Herrero-Albillos, *Phys. Rev. B* **2015**, *91*, 165111.
- [113] L. Rosado Piquer, E. Jiménez Romero, Y. Lan, W. Wernsdorfer, G. Aromí, E. C. Sañudo, *Inorg. Chem. Front.* **2017**, *4*, 595.
- [114] R. Baltic, F. Donati, A. Singha, C. Wäckerlin, J. Dreiser, B. Delley, M. Pivetta, S. Rusponi, H. Brune, *Phys. Rev. B* **2018**, *98*, 024412.
- [115] C.-H. Chen, L. Spree, E. Koutsouflakis, D. S. Krylov, F. Liu, A. Brandenburg, G. Velkos, S. Schimmel, S. M. Avdoshenko, A. Fedorov, E. Weschke, F. Choueikani, P. Ohresser, J. Dreiser, B. Büchner, A. A. Popov, *Adv. Sci.* **2021**, *8*, 2000777.
- [116] B. T. Thole, G. Van Der Laan, J. C. Fuggle, G. A. Sawatzky, R. C. Karnatak, J.-M. Esteve, *Phys. Rev. B* **1985**, *32*, 5107.
- [117] C. L. Melcher, S. Friedrich, S. P. Cramer, M. A. Spurrier, P. Szupryczynski, R. Nutt, *IEEE Trans Nucl Sci* **2005**, *52*, 1809.
- [118] H. B. Vasili, B. Casals, R. Cichelero, F. Macià, J. Geshev, P. Gargiani, M. Valvidares, J. Herrero-Martin, E. Pellegrin, J. Fontcuberta, G. Herranz, *Phys. Rev. B* **2017**, *96*, 014433.
- [119] P. Carra, B. T. Thole, M. Altarelli, X. Wang, *Phys. Rev. Lett.* **1993**, *70*, 694.
- [120] S. Tripathi, XMCD investigation at M<sub>4,5</sub> edges of the rare earth elements in high-performance permanent magnet. (Max-Planck-Institut für Intelligente Systeme, Stuttgart) 2018.
- [121] A. Tcakeev, V. B. Zabolotnyy, C. I. Fornari, P. Rüßmann, T. R. F. Peixoto, F. Stier, M. Dettbarn, P. Kagerer, E. Weschke, E. Schierle, P. Bencok, P. H. O. Rappl, E. Abramof, H. Bentmann, E. Goering, F. Reinert, V. Hinkov, *Phys. Rev. B* **2020**, *102*, 184401.
- [122] M. A. Laguna-Marco, J. Chaboy, C. Piquer, *J. Appl. Phys.* **2008**, *103*, 07E141.
- [123] T. V. Kuznetsova, V. I. Grebennikov, E. G. Gerasimov, N. V. Mushnikov, *J. Magn. Magn. Mater.* **2017**, *440*, 50.
- [124] J. Dreiser, K. S. Pedersen, C. Piamonteze, S. Rusponi, Z. Salman, M. d. E. Ali, M. Schau-Magnussen, C. A. Thuesen, S. Piligkos, H. Weihe, H. Mutka, O. Waldmann, P. Oppeneer, J. Bendix, F. Nolting, H. Brune, *Chem. Sci.* **3**, 1024.
- [125] L. Badía-Romano, J. Rubín, F. Bartolomé, J. Bartolomé, J. Luzón, D. Prodius, C. Turta, V. Mereacre, F. Wilhelm, A. Rogalev, *Phys. Rev. B* **2015**, *92*, 064411.
- [126] Y. Lan, S. Klyatskaya, M. Ruben, O. Fuhr, W. Wernsdorfer, A. Candini, V. Corradini, A. Lodi Rizzini, U. Del Pennino, F. Troiani, L. Joly, D. Klar, H. Wende, M. Affronte, *J. Mater. Chem. C* **2015**, *3*, 9794.
- [127] E. Bartolomé, J. Bartolomé, S. Melnic, D. Prodius, S. Shova, A. Arauzo, J. Luzón, F. Luis, C. Turta, *Dalton Trans.* **2013**, *42*, 10153.